remote sensing

MDPI

Article

Beyond Coastal Validation: Resolving Storm-Time Sea Surface Height Variability with SWOT High-Resolution Observations

Emma Imen Turki *, Md Saiful Islam, Carlos Lopez Solano, Mayowa Basit Abdulsalam and Amelie Arias

Univ Rouen Normandie, Université Caen Normandie, CNRS, Normandie Univ, M2C UMR 6143, F-76000 Rouen, France; md-saiful.islam@univ-rouen.fr (M.S.I.); carlos.lopez-solano4@univ-rouen.fr (C.L.S.); mayowa-basit.abdulsalam@univ-rouen.fr (M.B.A.); amelie.arias@univ-rouen.fr (A.A.)
* Correspondence: imen.turki@univ-rouen.fr

Highlights

What are the main findings?

- SWOT HR reveals storm-time SSH heterogeneity, including spatial structures with distinct geometries and orientations across contrasting coastal sites.
- A ~0.5–1.0 km energetic SSH scale range is identified in all three coastal cases examined, with strongly site-dependent spatial organization.

What is the implication of the main finding?

- SWOT HR extends coastal altimetry beyond point validation by resolving the two-dimensional, multiscale organization of storm-time SSH.
- These observations provide new spatial constraints for coastal-process analysis, model validation, and data assimilation.

Abstract

Coastal water levels during storms result from interacting tides, storm surges, waves, currents, bathymetry, and coastal geometry, producing spatially heterogeneous responses that remain difficult to characterize from point observations alone. The Surface Water and Ocean Topography (SWOT) mission provides a new opportunity to investigate this complexity through wide-swath High-Resolution (HR) observations of sea surface height (SSH). Here, SWOT HR water levels are first evaluated against five tide gauges in the English Channel and subsequently analyzed at three contrasting sites, Cherbourg, Villers-sur-Mer, and Étretat, using complementary spatial and scale-resolved approaches. SWOT HR shows strong agreement with tide gauges at the best-performing sites, with RMSE values of approximately 0.11 m and correlations exceeding 0.99, while accuracy remains site-dependent. Beyond point-based validation, the two-dimensional HR fields reveal pronounced spatial heterogeneity, including localized and elongated SSH anomalies with distinct geometries and orientations. EOF decomposition shows that more than half of the variance remains beyond the first six modes at all three sites, highlighting the complexity of the HR spatial signal. The detrended SSH anomalies show organized spatial patterns, while their point-by-point linear correlations with radar backscatter (σ^0) remain close to zero. Across the three investigated coastal domains and two storm events, the two-dimensional wavelet analysis identifies enhanced SSH variability within an energetic scale range of approximately 0.5–1.0 km, although its intensity, spatial distribution, and organization differ substantially among sites. Comparison with independent wave, surface-current, and bathymetric fields further places these observations within contrasting hydrodynamic and morphological environments, suggesting that the observed sub-kilometer SSH variability may be associated with local coastal processes, although their individual contributions

Check for updates

Academic Editors: Weimin Huang, Chen Zhao and Xin Qiao

Received: 4 October 2026
Revised: 30 October 2026
Accepted: 31 October 2026
Published: 5 November 2026

Copyright: © 2026 by the authors. Licensee MDPI, Basel, Switzerland. This article is an open access article distributed under the terms and conditions of the Creative Commons Attribution (CC BY) license.

remain unresolved. . Together, these analyses demonstrate the added value of SWOT HR for resolving the two-dimensional, multiscale complexity of storm-time coastal SSH, providing new spatial information for investigating coastal dynamics and supporting high-resolution model validation and data assimilation.

Keywords: SWOT; coastal altimetry; storm events; spatial variability; coastal hydrodynamics

1. Introduction

Coastal zones are increasingly exposed to hazards associated with extreme sea-level events, including flooding, erosion, and overtopping. During storms, coastal water levels result from the combined influence of atmospheric pressure and wind-driven surge, astronomical tides, surface waves and wave setup, currents, and their interactions with bathymetry and coastal morphology [1,2]. These processes can generate pronounced spatial variability over relatively short distances, particularly in shallow and geometrically complex coastal environments. Resolving this spatial heterogeneity is therefore essential for understanding storm-driven coastal dynamics and improving the observation and prediction of extreme water levels [3–5].

Coastal sea level and storm surges have traditionally been monitored using tide gauges, which provide accurate and high-frequency water-level records but remain spatially discrete [6,7]. Satellite radar altimetry has extended these observations over larger spatial domains and enabled storm-related sea-level anomalies to be detected from space [8–13]. However, conventional nadir altimeters primarily sample the ocean along predefined ground tracks and remain limited in their ability to resolve the two-dimensional spatial organization of rapidly varying coastal water levels. Retrieval also becomes increasingly challenging toward the shoreline because of land contamination, rapidly varying bathymetry and sea state, and uncertainties in geophysical corrections [14–16]. Other satellite techniques, particularly synthetic aperture radar, provide high-resolution two-dimensional information on waves, currents, fronts, and sea-surface roughness, but do not directly measure sea-surface height (SSH). A key observational gap therefore remains between spatially discrete direct measurements of water level and high-resolution two-dimensional observations of other sea-surface properties.

The Surface Water and Ocean Topography (SWOT) mission represents a major advance in addressing this observational gap by combining direct altimetric measurements of water-surface elevation with wide-swath two-dimensional sampling. Launched in December 2022, SWOT uses the Ka-band Radar Interferometer (KaRIn) to provide wide-swath, two-dimensional measurements of water-surface elevation at spatial scales inaccessible to conventional nadir altimetry [17–20]. Its distinctive contribution for coastal applications therefore lies not simply in finer spatial sampling, but in providing direct access to the two-dimensional spatial organization of SSH over extended coastal domains. The scientific exploitation of these observations nevertheless requires careful consideration of the magnitude, scale dependence, and spatial correlation of KaRIn errors, particularly when interpreting fine-scale variability [21–25]. These issues become particularly important close to the coast, where heterogeneous hydrodynamics and coastal geometry are strongly manifested.

Recent studies nevertheless demonstrate the emerging capability of SWOT in complex coastal environments. In the hyper-tidal Bristol Channel–Severn River–Estuary system, Lichtman et al. [26] showed that SWOT captures complex two-dimensional water-level patterns while highlighting the influence of morphology, hydrodynamics, and spatial collocation on comparisons with point gauges. Along the west coast of Canada, Han

et al. [27] reported close agreement between daily SWOT sea-level observations and coastal tide gauges, further demonstrating the capability of wide-swath altimetry to capture coastal sea-level variability. Other studies have demonstrated the capability of SWOT to observe water-level variability under challenging nearshore and energetic conditions [28,29]. Of particular relevance to extreme events, Vega-Gimenez et al. [30] showed that SWOT can characterize the two-dimensional spatial footprint of storm-driven sea-level anomalies across contrasting coastal environments. Together, these studies demonstrate the potential of SWOT to move coastal altimetry beyond point-scale validation toward observation of the two-dimensional spatial structure of coastal water levels.

At finer scales, SWOT observations are also revealing spatial structures associated with surface-wave dynamics. Recent studies have demonstrated that KaRIn can resolve long surface waves and their transformations, including refraction, diffraction, reflection, and wavelength changes associated with propagation toward the coast [28,31–33]. These developments are particularly relevant because they demonstrate that physically meaningful information can be retained within the spatial structure of SWOT HR observations at sub-kilometer-to-kilometer scales.

However, an important gap remains between demonstrating accurate coastal water-level retrieval and exploiting the full two-dimensional spatial information contained in SWOT HR observations. The multiscale organization of storm-time coastal SSH has not yet been comprehensively characterized from unsmoothed HR observations. In particular, it remains unclear which spatial scales dominate storm-time HR variability, where these structures are localized within the two-dimensional coastal field, whether comparable energetic scales emerge across contrasting coastal environments, and how their spatial expression relates to local wave, current, bathymetric, and morphological conditions. Establishing the reliability of HR water levels against independent coastal observations also remains necessary before these fine-scale structures can be physically interpreted.

The English Channel provides an appropriate natural laboratory for addressing these questions. Its strong tidal dynamics, energetic wave conditions, complex bathymetry, and contrasting coastal configurations produce pronounced spatial variability in water levels and hydrodynamic processes [29]. The region therefore enables SWOT HR observations to be examined across environments ranging from the relatively open entrance of the Channel to shallow nearshore settings.

Building on these recent advances, this study investigates the capability and added value of SWOT HR observations for characterizing storm-time coastal SSH variability beyond conventional point-based validation. SWOT HR water levels are first evaluated against tide-gauge observations at five stations. The SWOT 250 m unsmoothed product is additionally examined at Cherbourg to assess whether the broader spatial organization identified from HR PIXC persists independently of the HR gridding approach. The two-dimensional HR fields are then analyzed at three contrasting sites, Cherbourg, Villers-sur-Mer, and Étretat, to: (1) characterize the spatial organization of storm-time SSH variability; (2) identify its dominant spatial scales and their localization; (3) examine potential physical contributions from wave dynamics and the surrounding hydrodynamic environment; and (4) determine how these structures vary across contrasting coastal configurations and storm conditions.

The remainder of this paper is organized as follows. Section 2 describes the study areas, datasets, and methodological approaches. Section 3 presents the validation of SWOT HR observations against tide gauges, followed by the analysis of storm-time SSH spatial variability using EOF decomposition and two-dimensional wavelet analysis. Section 4 discusses the spatial patterns identified, their potential physical interpretation, and the implications for coastal monitoring and modeling. Finally, Section 5 summarizes the main findings and outlines perspectives for future research.

2. Materials and Methods

2.1. Study Area and Selected Coastal Sites

The study focuses on the English Channel, an energetic macrotidal shelf sea connecting the North Atlantic Ocean to the North Sea (Figure 1). The region is characterized by strong semidiurnal tides, energetic wave conditions, spatially variable bathymetry, and complex interactions among tides, currents, waves, and coastal morphology. These processes generate pronounced spatial variability in coastal sea-surface height (SSH), particularly during energetic storm conditions [29]. The English Channel therefore provides a suitable natural setting for assessing the capability of SWOT high-resolution (HR) observations to resolve coastal water levels and storm-time SSH variability across contrasting hydrodynamic and coastal environments.

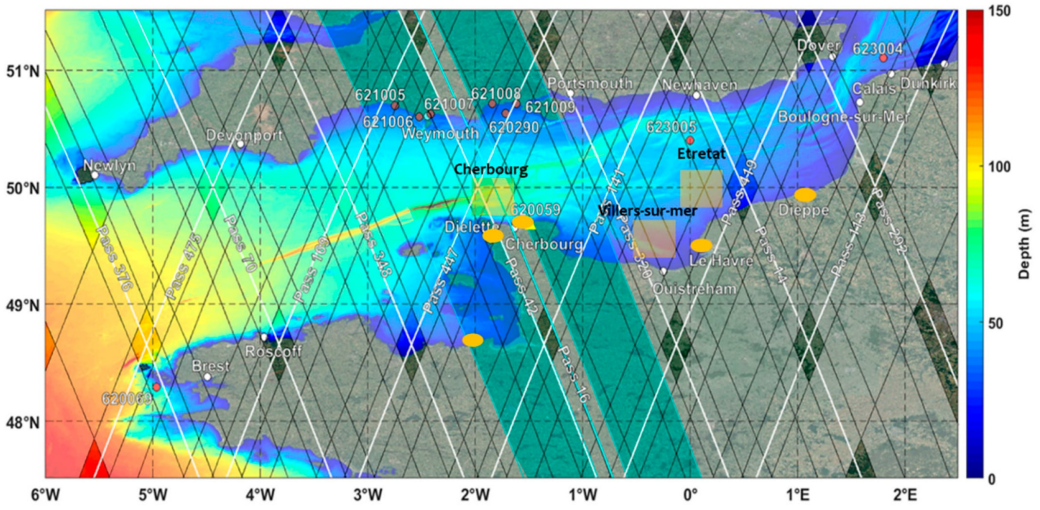


Figure 1. Study area and SWOT ground-track coverage in the English Channel. Bathymetry is shown alongside SWOT ground tracks (gray color, with the Cal/Val pass highlighted in green), tide-gauge stations (yellow oval forms) used for validation, and the three coastal study sites (Cherbourg, Villers-sur-Mer, and Étretat, yellow square forms).

The analysis is conducted at two complementary spatial levels. First, SWOT HR coastal water levels are evaluated against tide-gauge observations at five stations distributed along the English Channel (Dieppe, Le Havre, Cherbourg, Dielette, Saint Malo), providing a regional assessment of SWOT performance close to the coast. The locations of the five stations and the corresponding SWOT ground tracks are shown in Figure 1. This regional validation provides the basis for assessing the reliability of the HR water-level observations before exploiting their finer-scale two-dimensional spatial information.

Second, three sites, Cherbourg (entrance of the Channel), Villers-sur-Mer, and Étretat (Normandy Coasts) were selected for detailed two-dimensional analysis of storm-time SWOT HR observations. The sites span contrasting coastal configurations and bathymetric settings. Cherbourg is characterized by complex coastal geometry and strong tidal dynamics; Villers-sur-Mer represents a shallow macrotidal environment within the Bay of Seine; and Étretat corresponds to a more exposed coastal setting with contrasting nearshore morphology and bathymetry. Together, these sites provide a framework for examining how the spatial structures resolved by SWOT HR vary across contrasting coastal and hydrodynamic environments.

The selected SWOT acquisitions coincide with two energetic storm events. SWOT observations over Villers-sur-Mer and Étretat were acquired during Storm Benjamin on 29 October 2025, allowing contrasting coastal configurations to be examined under the same storm forcing. The Cherbourg acquisition corresponds to Storm Chandra on 26 January

2026 and provides a complementary case under different coastal, hydrodynamic, and storm conditions. The main meteorological and oceanographic characteristics of the two events, together with the corresponding SWOT acquisition information, are summarized in Table 1.

Table 1. Characteristics of the storm events and corresponding SWOT HR acquisitions selected for detailed spatial analysis at Cherbourg, Villers-sur-Mer, and Étretat.

STORM	Site	SWOT Sampling Pass/Cycle Number	Energy (m^2/h)	Hs (Max), (m)	Duration (Days)
Chandra 25 January 2026	Cherbourg	Pass 42, cycle 45	3088	9.9	3.79
Benjamin 26 October 2025	Villers-sur-mer Etretat	Pass 419, cycle 40	258	3.5	1.96

This experimental configuration enables complementary analyses of coastal water-level accuracy and fine-scale spatial variability: a five-station regional validation of SWOT HR close to the coast, a cross-site comparison of Villers-sur-Mer and Étretat under a common storm event, and a broader comparison with Cherbourg under different coastal and storm conditions. It therefore provides a basis for investigating the added value of unsmoothed SWOT HR observations and how the characteristic spatial structures and wavelengths they resolve vary with coastal configuration, bathymetry, hydrodynamic setting, and storm forcing.

2.2. SWOT HR PIXC Data and Preprocessing

This study uses high-resolution (HR) observations from the Surface Water and Ocean Topography (SWOT) mission, launched in December 2022 by NASA and CNES, with contributions from the Canadian and UK space agencies. SWOT introduces two-dimensional wide-swath altimetry through the Ka-band Radar Interferometer (KaRIn), which observes two swaths on either side of the nadir track. Each swath is approximately 50 km wide and is separated from the other by a nadir gap of approximately 20 km, with near-nadir incidence angles ranging from approximately 0.6° to 4°. In contrast to conventional nadir altimetry, this observing geometry provides spatially distributed measurements of water-surface elevation and radar backscatter, enabling the two-dimensional characterization of sea-surface height (SSH) variability.

The analysis is based on the Level-2 KaRIn High-Rate Pixel Cloud product (L2_HR_PIXC), Version D [34]. The HR PIXC product is generated over a reloadable water mask covering inland and coastal waters and was selected because it provides measurements at the native pixel level within the nearshore zone of the English Channel. Each granule consists of an unstructured cloud of geolocated water pixels within a swath-aligned tile of approximately 64 × 64 km associated with the left or right side of a SWOT overpass. The nominal along-track posting is approximately 22 m, while the ground area represented by individual measurements varies across the swath, with spatial sampling becoming coarser from near to far range. The designation pixel cloud reflects this spatially variable measurement geometry.

SWOT HR coastal water levels were evaluated against tide-gauge observations at five stations distributed along the French coast of the English Channel: Saint-Malo, Diélette, Cherbourg, Le Havre, and Dieppe (Figure 1).

For each classified water pixel, the PIXC product provides geodetic coordinates, ellipsoidal water-surface height referenced to the WGS84 ellipsoid, normalized radar backscatter coefficient (σ^0), surface classification, geophysical corrections, and associated quality information. The PIXC product was preferred over spatially smoothed or lower-resolution

gridded SWOT products because the objectives of this study require preservation of the fine-scale spatial information contained in the HR observations. Retaining this information is particularly important for identifying localized SSH structures, determining their characteristic spatial wavelengths, and assessing the added value of unsmoothed SWOT HR observations for characterizing storm-time coastal variability.

For the selected storm acquisitions, the corresponding PIXC tiles and swaths were extracted over the English Channel, and site-specific subsets were subsequently defined around Cherbourg, Villers-sur-Mer, and Étretat. For each site, a 10 × 10 km coastal domain was selected to provide a common spatial framework for the two-dimensional analyses. The domains were positioned to retain sufficient valid SWOT water observations while sampling the nearshore zone and limiting areas dominated by land or insufficient observational coverage. Figure 2 presents the native PIXC observations over the three domains in terms of ellipsoidal height and σ^0.

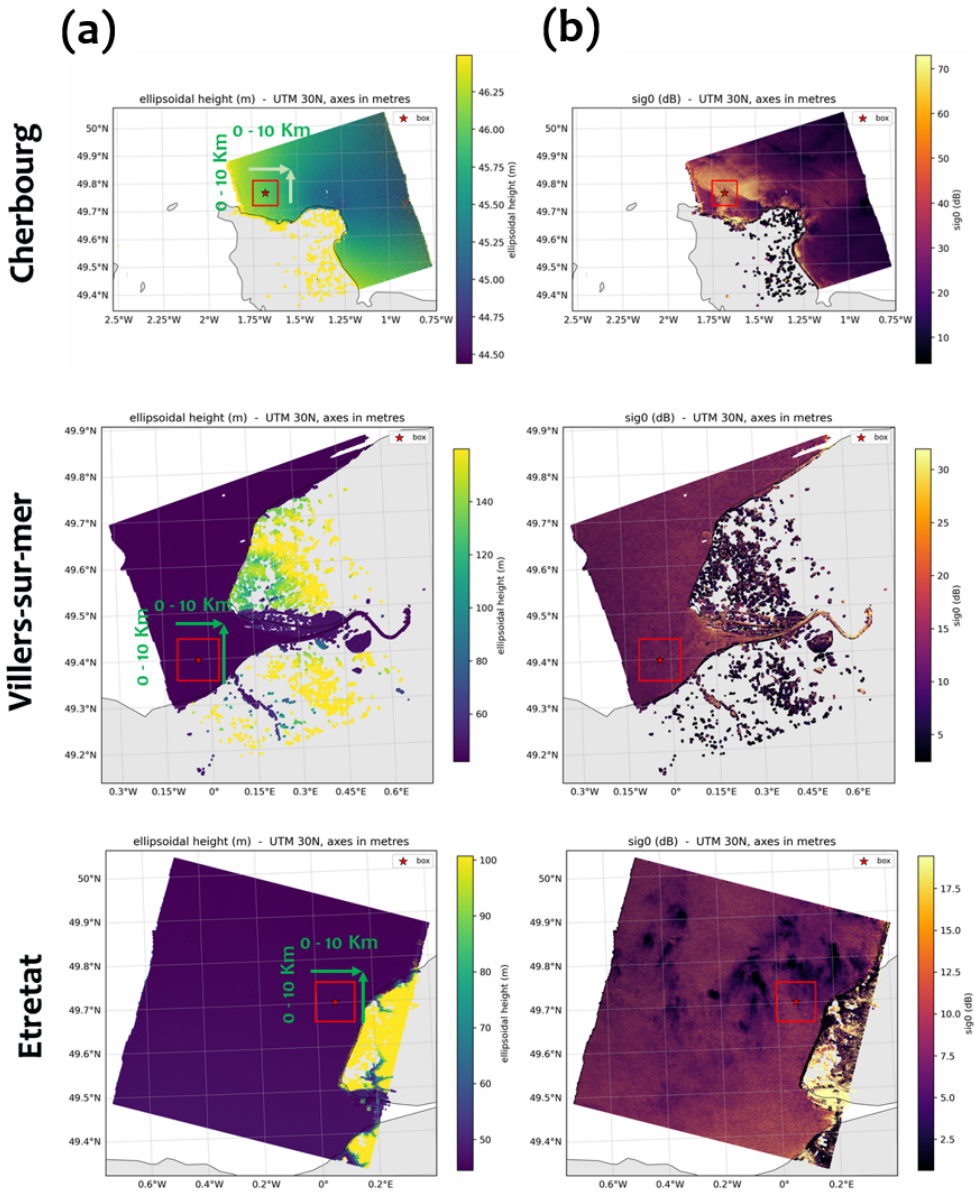


Figure 2. SWOT HR observations at the three selected coastal sites: Cherbourg, Villers-sur-Mer, and Étretat. Panels in (**a**) show SWOT HR PIXC ellipsoidal height, while panels in (**b**) show radar backscatter (σ^0). Red boxes indicate the 10 × 10 km domains selected for detailed spatial analysis. The arrows indicate the direction of increasing distance along the transects, from 0 to 10 km.

Because the native PIXC measurements are irregularly distributed, valid observations within each 10 × 10 km domain were interpolated onto a regular Cartesian grid with a 50 m spacing using linear interpolation. This common grid provides the two-dimensional fields required for the subsequent spatial and multiscale analyses. The 50 m spacing represents the sampling interval of the analysis grid and should not be interpreted as the effective independent spatial resolution of KaRIn. Areas without PIXC observational coverage were masked and excluded from further analysis. No additional spatial smoothing was applied. However, interpolation may influence the amplitude and spatial organization of fine-scale SSH variability, particularly in areas with sparse observations. This potential effect is considered when interpreting the spatial and wavelet analyses.

Native PIXC samples are irregularly distributed in ground coordinates. Pixels flagged as bad in the geolocation quality flag were discarded, and the remaining samples were projected to the UTM zone. Within each 10 × 10 km domain, heights were then averaged into 50 × 50 m cells. The 50 m spacing defines the sampling interval of the analysis grid and should not be interpreted as the effective independent spatial resolution of KaRIn. Cell averaging acts as a 50 m boxcar filter, which reduces pixel-level noise while attenuating wavelengths $\geq$ 300 m by less than 5%; no further smoothing was applied. A quadratic surface, fitted by least squares to observed cells only, was removed to suppress large-scale gradients from the geoid, tides and residual geophysical corrections. Small gaps of $\leq$25 contiguous cells ($\leq$0.0625 km^2), attributable to irregular sampling rather than missing coverage, were filled by linear interpolation of the detrended field. Larger gaps and cells outside the convex hull of the observations were masked as NaN and excluded from the analysis. Because interpolated cells carry less variance than observed ones, they were excluded from the computation of spectral energy and variance statistics.

In addition to SSH, σ^0 was retained as complementary information on spatial variations in radar backscatter and surface roughness. The σ^0 observations were mapped onto the same 50 m analysis grid as SSH, allowing their spatial distribution to be examined consistently across Cherbourg, Villers-sur-Mer, and Étretat. In particular, σ^0 was used to assess whether the fine-scale spatial variability identified in the SSH fields was associated with corresponding variations in radar backscatter. σ^0 is therefore considered here as a complementary indicator of surface-state variability rather than as a direct quantitative measure of wave characteristics. The quantitative correspondence between σ^0 and the detrended SSH spatial anomalies is described in Section 2.5.

For complementary comparison, the corresponding SWOT 250 m unsmoothed product was also examined to assess the extent to which the fine-scale coastal SSH structures identified in the HR observations remain detectable at coarser spatial sampling.

2.3. SWOT HR Validation Methodology

The performance of SWOT HR PIXC observations close to the coast was evaluated against tide-gauge measurements at five stations distributed along the French coast of the English Channel: Saint-Malo, Diélette, Cherbourg, Le Havre, and Dieppe (Figure 1). The validation was designed to provide an independent assessment of the reliability of the coastal water-level measurements before exploiting the two-dimensional HR fields for the subsequent spatial and multiscale analyses. For each station, SWOT HR PIXC observations were spatially collocated with the tide-gauge location and temporally matched with the corresponding in situ water-level measurement at the SWOT acquisition time. Only valid water pixels satisfying the adopted PIXC classification and quality criteria were retained. SWOT and tide-gauge measurements were expressed as ellipsoidal heights within a common vertical reference, allowing direct comparison of the satellite and in situ water levels.

The SWOT Level-3 250 m Unsmoothed v2.0.1 product (AVISO/DUACS, 2024a, 2024b) was additionally used at Cherbourg to provide an independent representation of the spatial water-level field without the 50 m gridding applied to the HR PIXC observations. The product was used without additional spatial smoothing or interpolation, allowing assessment of whether the broader SSH spatial organization identified from HR PIXC remains detectable at the 250 m product scale.

2.4. EOF Decomposition of Spatial SSH Variability

Empirical orthogonal function (EOF) analysis was applied to the original two-dimensional SWOT HR SSH fields to characterize the dominant spatial organization of water-level variability at each study site. The objective of this analysis was not to remove individual EOF modes from the observations, but rather to quantify how the spatial variance of the SSH field is distributed among a limited number of orthogonal patterns before performing the subsequent multiscale analysis.

For each 10 × 10 km domain, the gridded SSH field was first represented as a spatial data matrix. Missing values were treated consistently with the preprocessing described above, and the spatial mean was removed prior to decomposition. The resulting mean-centered SSH matrix was decomposed using singular value decomposition (SVD), allowing the SSH variability to be expressed as a linear combination of orthogonal spatial modes.

$$X = U \sum V^T \tag{1}$$

where U and V contain the orthogonal modes and Σ contains the corresponding singular values. The relative contribution of each mode to the total variance was estimated from the associated eigenvalues.

$$EV_i = \frac{\lambda_j}{\sum_{j-1}^{N} \lambda_j} \times 100 \tag{2}$$

where EV_i is the percentage of variance explained by the *Ith* EOF mode and λ_i is its corresponding eigenvalue.

The first six EOF modes (EOF_1–EOF_6) were retained for comparative analysis at Cherbourg, Villers-sur-Mer, and Étretat. Their spatial patterns and explained-variance contributions were used to assess whether the original storm-time SSH fields were dominated by a leading coherent spatial structure or characterized by a more distributed contribution from higher-order modes. No EOF mode was removed from the SSH field on the basis of this decomposition. Instead, the EOF analysis was used as an independent diagnostic of spatial variance organization, while removal of the large-scale spatial background for the subsequent spectral analysis was performed separately using a two-dimensional planar detrending procedure (Section 2.5).

2.5. Extraction of the Detrended SSH Spatial Anomaly

Prior to the multiscale analysis, the large-scale spatial background was removed from each SWOT HR SSH field in order to isolate the spatial variability superimposed on the regional water-level gradient. This step was performed independently of the EOF decomposition described above and was designed to prevent the dominant large-scale spatial gradient of the SSH field from overwhelming the spectral signature of shorter spatial structures. For each 10 × 10 km analysis domain, a first-order two-dimensional plane was fitted to the gridded SSH field:

$$\eta_{plane}(x, y) = a + bx + cy \tag{3}$$

where x and y are the Cartesian spatial coordinates, $\eta_{plane}(x,y)$ is simply the fitted large-scale planar background of the SSH field, a is the intercept, and a, b and c represent the large-scale

SSH gradients along the two horizontal directions. The coefficients were estimated using the valid SWOT HR observations within each domain.

The detrended SSH spatial anomaly, hereafter denoted $\eta'(x,y)$, was then calculated as

$$\eta'(x,y) = \eta(x,y) - \eta_{bg}(x,y) \quad (4)$$

where $\eta(x,y)$ is the original SWOT HR SSH field. This operation removes the first-order spatial background while retaining shorter-scale departures from that background.

The detrending was applied consistently to the Cherbourg, Villers-sur-Mer, and Étretat domains. Limited internal gaps in the gridded fields were interpolated prior to the spectral analysis, whereas regions without sufficient observational support were excluded. The resulting detrended fields constitute the input to the two-dimensional Morlet wavelet analysis described in Section 2.6. Importantly, $\eta'(x,y)$ is referred to here as a spatial SSH anomaly and should not be interpreted as a conventional temporal sea-level anomaly relative to a climatological or tidal reference. It represents the departure of the instantaneous SWOT HR SSH field from its locally fitted large-scale spatial background.

To assess whether the fine-scale SSH variability was directly associated with spatial variations in radar backscatter, the correspondence between $\eta'(x,y)$ and σ^0 was quantified independently for Cherbourg, Villers-sur-Mer, and Étretat. Pearson correlation coefficients were calculated using co-located valid observations on the common 50 m grid. The resulting coefficients were interpreted as descriptive measures of point-by-point spatial co-variability rather than as evidence of a causal relationship. The correlation analysis was considered together with the corresponding two-dimensional σ^0 distributions and independent wave and hydrodynamic information in the subsequent physical interpretation.

2.6. Wavelet Analysis of Detrended SSH Spatial Anomalies

A two-dimensional continuous wavelet transform (2-D CWT) based on the Morlet wavelet was applied to the detrended SWOT HR SSH anomalies to characterize their multiscale spatial variability. Unlike a global spectral decomposition, the wavelet approach preserves spatial localization, allowing both the characteristic wavelengths of SSH variability and their position within each coastal domain to be identified. For each spatial wavelength λ, local wavelet power was calculated as

$$P(x,y,\lambda) = W\big(x,y,\lambda\big)^2 \quad (5)$$

where $W(x,y,\lambda)$ denotes the complex Morlet wavelet coefficient. The spatially averaged wavelet power was used to identify energetic wavelength ranges, while two-dimensional power maps and three-dimensional scale–space representations were used to examine their spatial localization and evolution across scales.

Because the spatial support of the wavelet increases with wavelength, boundary effects become progressively more important at larger scales. An edge-exclusion criterion was therefore applied at each wavelength, and the fraction of the domain remaining valid was evaluated jointly with the global wavelet power. Scale-integrated wavelet power was subsequently calculated over selected wavelength bands to identify regions where scale-dependent SSH variability was concentrated. Additional details on the wavelet analysis and the treatment of boundary effects are provided in Appendix A.

The analysis is entirely spatial: λ denotes the spatial scale associated with the Morlet wavelet rather than a temporal frequency or period. The detected energetic scales characterize the dimensions and localization of organized SSH variability but should not be interpreted as direct measurements of individual surface-wave wavelengths or as evidence of a particular physical mechanism. Their possible physical interpretation is subsequently discussed in relation to bathymetry and modeled wave, surface-current, and water-level conditions.

2.7. Environmental and Hydrodynamic Conditions During SWOT Acquisitions

Hydrodynamic and wave conditions associated with the SWOT acquisitions were characterized using model and environmental fields available from different platforms. Wave conditions were obtained from the NWShelf wave reanalysis distributed by the Copernicus Marine Service, with fields corresponding as closely as possible to the SWOT acquisition times extracted over the three study sites. Surface currents were obtained from the MARC MARS3D (Model for Applications at Regional Scale) model developed by IFREMER, with a spatial resolution of 2.5 km, while bathymetric data were obtained from EMODnet. Wave conditions, surface currents, water levels, and bathymetry were used as independent environmental information to support the physical interpretation of the spatial structures and scale-dependent variability identified in the SWOT HR observations. These fields were not used to validate or attribute the wavelet-derived scales to specific physical processes, but rather to examine whether their spatial expression was consistent with the prevailing wave forcing, current structure, bathymetric setting, and coastal configuration during the SWOT acquisitions.

3. Results

3.1. Validation of SWOT HR in Coastal Waters

3.1.1. SWOT HR–Tide Gauge Agreement

SWOT HR PIXC water-level observations were evaluated against temporally matched tide-gauge measurements at five stations distributed along the English Channel (Figure 3). Overall, SWOT HR shows strong agreement with in situ water levels, although the performance varies among stations. The highest agreement was obtained at Cherbourg and Le Havre. At Cherbourg, 21 matched observations yield a correlation coefficient of r = 0.9969, an RMSE of 0.111 m, and a negligible bias of −0.010 m. The regression slope of 0.977 is close to unity, indicating that both the magnitude and variability of the observed water levels are well reproduced by SWOT HR. Similarly, Le Havre shows excellent agreement for 25 matched observations, with r = 0.9988, an RMSE of 0.106 m, and essentially zero bias. The regression slope of 1.007 closely follows the 1:1 relationship. Good agreement is also obtained at Saint-Malo and Diélette, although with greater dispersion. At Saint-Malo, 25 matched observations yield r = 0.986, an RMSE of 0.527 m, and a positive bias of 0.130 m. At Diélette, the correlation remains high (r = 0.9189; $N = 24$), while the RMSE increases to 0.858 m and the bias to 0.230 m. The corresponding regression slopes of 0.894 and 0.767 indicate increasing departures from the 1:1 relationship compared with Cherbourg and Le Havre. Dieppe exhibits a markedly different behavior. Although the correlation remains positive (r = 0.825, $N = 25$), the comparison shows substantially greater dispersion, with an RMSE of 2.8 m, a standard deviation of 2.721 m, and a positive bias of 0.945 m. Several SWOT observations strongly depart from the corresponding tide-gauge measurements, resulting in a regression slope of 1.360. The validation therefore reveals a clear site dependence in SWOT HR coastal performance, with very high accuracy at Cherbourg and Le Havre, good correlation but increased errors at Saint-Malo and Diélette, and substantial degradation at Dieppe. Taken together, these results demonstrate that SWOT HR can reproduce coastal water-level variability with strong agreement at four of the five investigated sites, while also highlighting substantial local variability in retrieval performance. This validation provides the basis for subsequently exploiting the two-dimensional HR observations to investigate spatial water-level variability beyond the point-scale information provided by tide gauges.

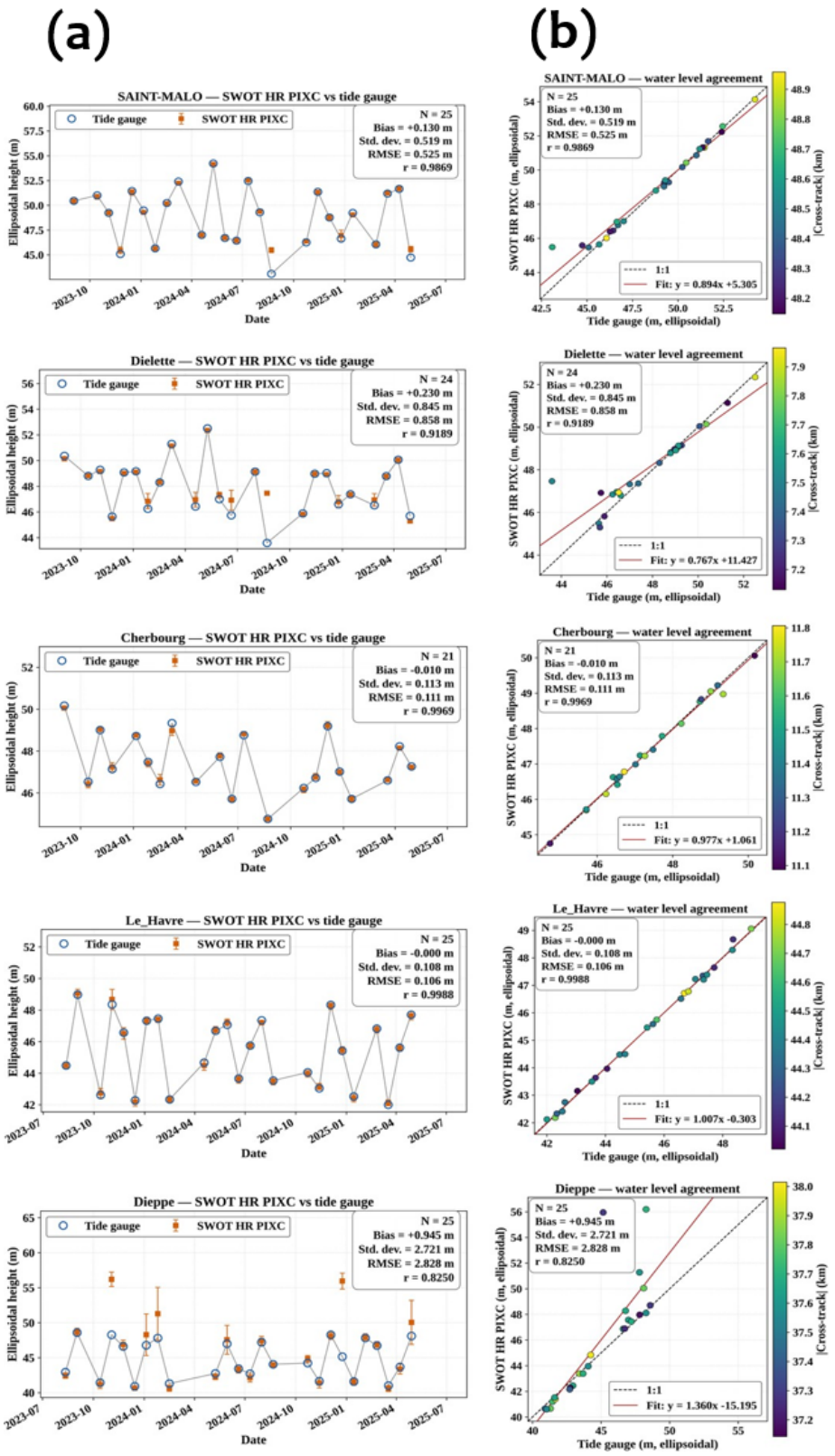


Figure 3. Validation of SWOT HR PIXC water levels against tide-gauge observations at five English Channel stations: Saint-Malo, Diélette, Cherbourg, Le Havre, and Dieppe (top to bottom). Panels (**a**) compare temporally matched SWOT and tide-gauge ellipsoidal heights, with error bars indicating the spatial variability of the collocated SWOT observations. Panels (**b**) show the corresponding scatterplots, including the 1:1 relationship (dashed line), linear regression (red line), and validation statistics. Colors indicate the SWOT cross-track position.

3.1.2. Spatial Variability in Validation Performance

Beyond the overall agreement with tide-gauge observations, the validation metrics reveal pronounced spatial variability in SWOT HR performance across the investigated coastal sites. RMSE ranges from approximately 0.11 m at Cherbourg and Le Havre to 2.83 m at Dieppe, while the bias varies from nearly zero at the best-performing sites to +0.95 m at Dieppe. The simultaneous increase in RMSE and bias, together with the decrease in correlation at the less consistent sites, indicates that the observed differences cannot be explained by a uniform vertical offset alone.

The validation performance therefore exhibits a clear site dependence, with substantial differences in accuracy among the five coastal stations. These differences may reflect variations in the local observation environment, including the spatial distribution of valid PIXC observations and coastal configuration, but their respective contributions are not isolated here. The results emphasize that SWOT HR performance close to the coast cannot be represented by a single accuracy estimate and should instead be considered in relation to the local coastal setting.

3.2. Spatial Organization of Storm-Time Coastal SSH

3.2.1. EOF Decomposition Across Contrasting Coastal Settings

Following the validation of SWOT HR observations, EOF decomposition was used to characterize the spatial organization of storm-time SSH variability across the three study domains. The selected sites represent contrasting sectors of the English Channel. Cherbourg is located near the western entrance of the Channel, in a relatively deeper and more open setting exposed to incoming storm-wave conditions, whereas Villers-sur-Mer and Étretat are located farther east in shallower coastal environments, where the wave field reaching the coast has undergone a longer propagation through the Channel and increasingly modified by bathymetry, tidal currents, and coastal geometry. Villers-sur-Mer and Étretat were observed during the same Storm Benjamin acquisition, whereas Cherbourg was sampled during Storm Chandra. The EOF analysis therefore provides a common framework for examining the spatial organization of the HR SSH fields across contrasting coastal settings and storm conditions. For each domain, the EOF decomposition was examined in terms of the spatial structure and relative contribution of the leading modes. Only modes explaining more than 1% of the total SSH variance were retained for detailed interpretation. Rather than considering the dominant mode alone, the analysis evaluates how the variance is partitioned among the significant EOF components and how their spatial patterns differ among the three domains.

At Cherbourg (Figure 4), EOF_1 accounts for 37.8% of the total SSH variance and displays a spatially coherent pattern extending across most of the domain. The subsequent significant modes contribute individually only 1.6–2.4% and exhibit more heterogeneous, alternating spatial structures. At Villers-sur-Mer (Figure 5), EOF_1 explains 24.7% of the variance and is characterized by a broad spatial gradient across the domain. The higher-order significant modes contribute 1.7–2.2% individually and display more heterogeneous and localized spatial patterns. At Étretat (Figure 6), EOF_1 accounts for 37.5% of the variance and similarly exhibits a broad, spatially coherent gradient across the domain. The subsequent significant modes contribute 1.6–2.4% individually and show weaker, more spatially heterogeneous structures.

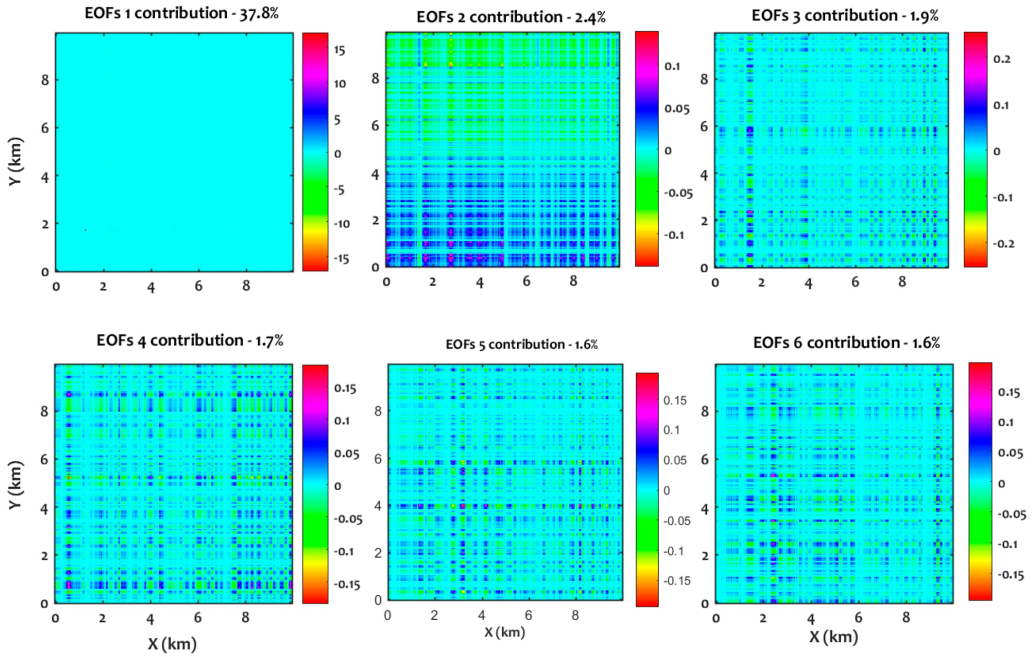


Figure 4. EOF decomposition of the original SWOT HR sea surface height field at Cherbourg. Spatial patterns of the first six empirical orthogonal function (EOF) modes derived from the original two-dimensional SWOT HR SSH field. The percentage indicated above each panel represents the fraction of total variance explained by the corresponding mode. EOF_1 accounts for 37.8% of the variance, followed by a marked decrease in the contribution of the higher-order modes, revealing a dominant large-scale component superimposed on weaker spatial variability.

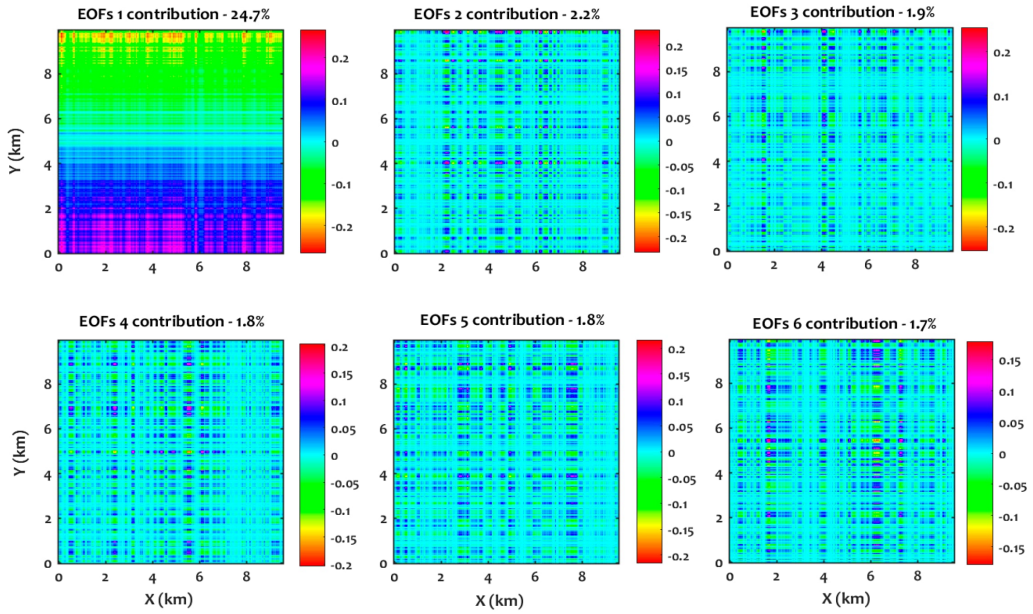


Figure 5. EOF decomposition of the original SWOT HR sea surface height field at Villers-sur-mer. Spatial patterns of the first six empirical orthogonal function (EOF) modes derived from the original two-dimensional SWOT HR SSH field. The percentage indicated above each panel represents the fraction of total variance explained by the corresponding mode. EOF_1 accounts for 24.7% of the variance, followed by a marked decrease in the contribution of the higher-order modes, revealing a dominant large-scale component superimposed on weaker spatial variability.

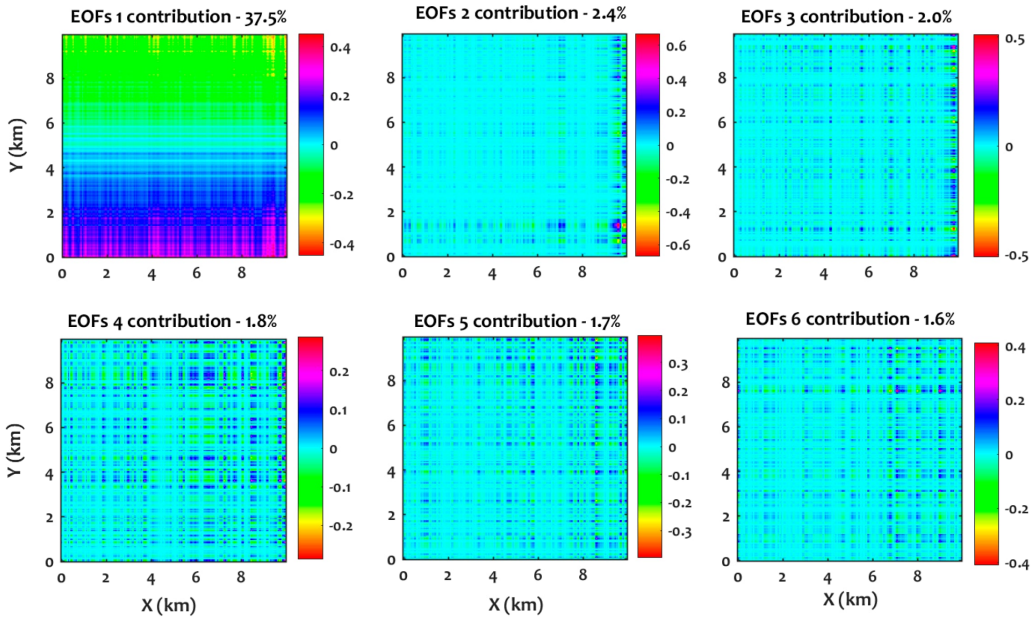


Figure 6. EOF decomposition of the original SWOT HR sea surface height field at Etretat. Spatial patterns of the first six empirical orthogonal function (EOF) modes derived from the original two-dimensional SWOT HR SSH field. The percentage indicated above each panel represents the fraction of total variance explained by the corresponding mode. EOF_1 accounts for 37.5% of the variance, followed by a marked decrease in the contribution of the higher-order modes, revealing a dominant large-scale component superimposed on weaker spatial variability.

3.2.2. Cross-Site Variability in Spatial Organization

Comparison of the EOF decompositions reveals marked differences in the partitioning of SSH variance among the three domains (Table 2). The leading mode accounts for 37.8% of the total variance at Cherbourg and 37.5% at Étretat, but only 24.7% at Villers-sur-Mer. When the first six modes are considered together, they explain 47.0% of the variance at both Cherbourg and Étretat, compared with 34.1% at Villers-sur-Mer. Consequently, 65.9% of the variance at Villers-sur-Mer remains distributed beyond the first six modes, compared with 53.0% at the other two sites. The contrast between Villers-sur-Mer and Étretat is particularly noteworthy because both domains were observed during the same Storm Benjamin acquisition. Despite being subjected to the same regional storm event, the two coastal domains exhibit different variance partitioning: Étretat retains a comparatively strong leading spatial component, whereas the lower contribution of EOF_1 and of the first six modes at Villers-sur-Mer indicates a more broadly distributed spatial variability. This difference demonstrates that the spatial organization resolved by SWOT HR can vary substantially between coastal environments even during the same storm event. Cherbourg, observed during Storm Chandra, shows a variance partitioning similar to Étretat, with EOF1 explaining 37.8% and 37.5% of the total variance, respectively, and the first six modes accounting for 47.0% at both sites. However, the two sites were observed during different storm events and represent contrasting coastal settings. Their similar EOF variance partitioning therefore indicates a comparable degree of spatial organization, although the processes shaping this organization may differ between the two sites. Overall, the EOF analysis demonstrates that storm-time SSH variability is organized differently across the investigated domains, motivating the subsequent analysis of the detrended SSH anomalies and their characteristic spatial scales.

Table 2. Cross-site comparison of EOF variance partitioning for the SWOT HR SSH fields. EOF1 represents the variance explained by the leading mode, EOF2–6 their cumulative contribution, and "Beyond first 6" the remaining variance.

Site	Coastal Setting	EOF_1	$EOF_{2–6}$	First 6 EOFs	Beyond First 6
Cherbourg	More open/deeper	37.8%	9.2%	47.0%	53.0%
Villers-sur-Mer	Shallow coastal	24.7%	9.4%	34.1%	65.9%
Étretat	Shallow coastal	37.5%	9.5%	47.0%	53.0%

3.3. Storm-Time SSH Spatial Anomalies

The EOF decomposition showed that storm-time SSH variability comprises a leading spatial component together with substantial higher-order variability. To isolate the shorter-scale spatial structures from the broad background organization, a first-order two-dimensional trend was removed from each SWOT HR SSH field. The resulting anomaly fields reveal pronounced spatial heterogeneity across all three domains, with alternating positive and negative anomalies whose geometry and distribution vary among the sites (Figure 7). At Cherbourg (Figure 7, upper panel), the original SSH field exhibits substantial spatial variability superimposed on a broad variation across the 10 × 10 km domain. After detrending, the residual field remains highly structured, with numerous elongated anomalies distributed throughout the domain. Several of these structures exhibit a clear oblique orientation that varies spatially across the domain (red arrows in Figure 7, upper panel). This organized directional pattern indicates that the residual variability is not randomly distributed. Its persistence after removal of the planar background further demonstrates that the observed HR spatial heterogeneity is not solely associated with the large-scale SSH gradient.

Similar changes in the spatial organization of the residual patterns are also observed at Étretat (Figure 7, lower panel). After removal of the broad spatial background, the anomaly field remains highly structured, with numerous elongated positive and negative features exhibiting preferential oblique orientations. The orientation of these structures varies across the domain, as highlighted by the red arrows, indicating that the directional organization is not spatially uniform. As at Cherbourg, these patterns persist after detrending, confirming that they are embedded within the residual HR SSH variability rather than being associated solely with the large-scale spatial gradient.

At Villers-sur-Mer (Figure 7, middle panel), detrending similarly reveals substantial residual SSH variability across the domain. However, unlike Cherbourg and Étretat, no clear preferential orientation of the anomaly structures is identified. The positive and negative anomalies appear more spatially dispersed, with heterogeneous structures distributed throughout the domain rather than organized along a persistent direction. This more distributed spatial organization is consistent with the weaker dominance of EOF1 identified at Villers-sur-Mer.

Overall, Figure 7 demonstrates that removal of the large-scale background does not eliminate the spatial organization of the SWOT HR fields. Substantial residual variability persists at all three sites, while its geometry and directional organization differ among the domains. Cherbourg and Étretat exhibit clearly elongated, locally oriented structures, whereas Villers-sur-Mer is characterized by a more dispersed and heterogeneous anomaly field. These differences complement the EOF results and demonstrate that storm-time HR variability cannot be characterized solely by the contribution of a few dominant spatial modes. However, neither the EOF decomposition nor the anomaly maps alone establish whether these residual SSH structures are associated with variations in radar backscatter, nor do they provide a quantitative measure of their characteristic spatial scales. These

results therefore motivate further examination of the residual SSH variability to determine whether its spatial organization is associated with variations in radar backscatter and to quantify the characteristic spatial scales embedded within the observed structures.

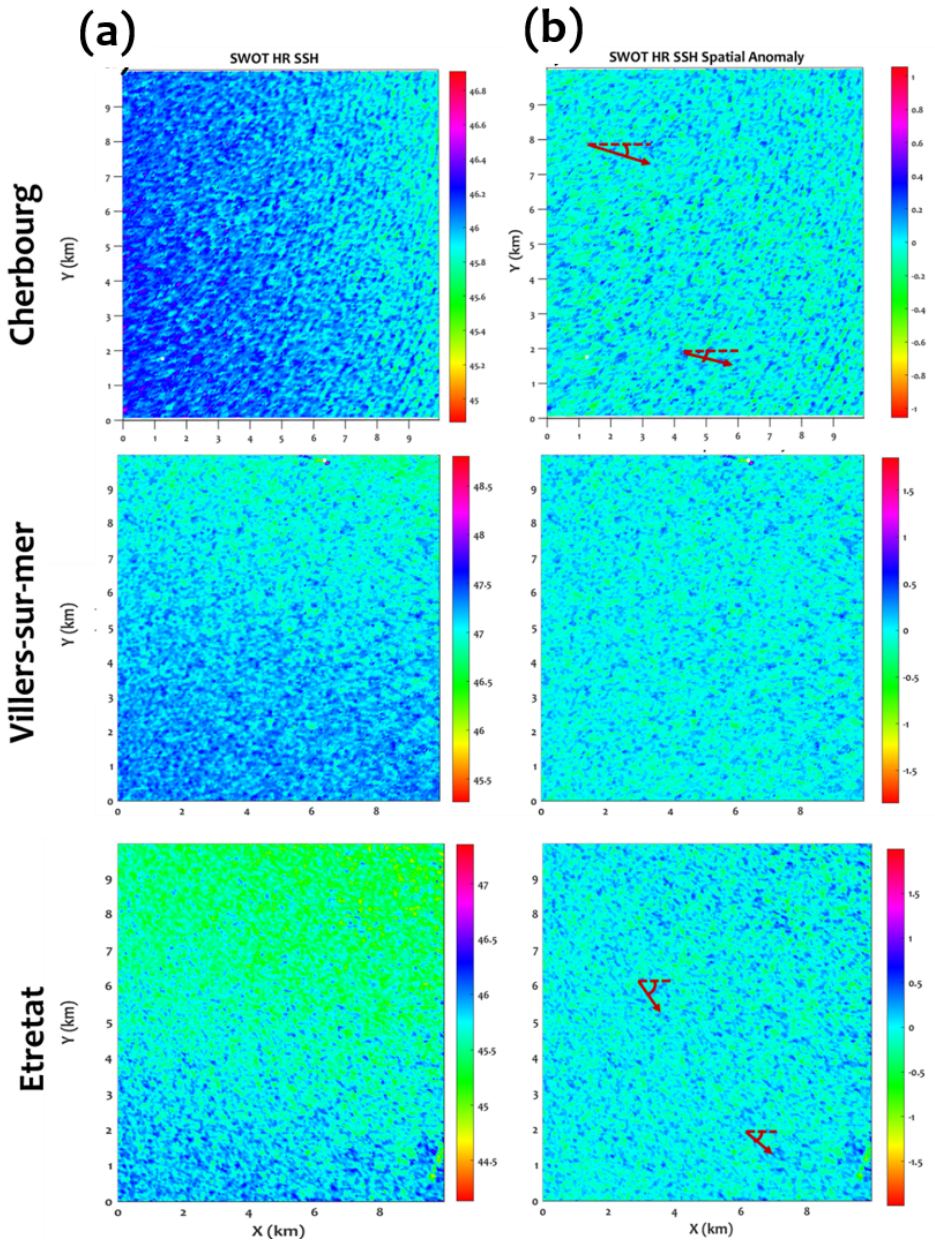


Figure 7. Original (**a**) and detrended (**b**) SWOT HR SSH fields for Cherbourg (**upper panels**), Villers-sur-Mer (**middle panels**), and Étretat (**lower panels**). The detrended fields represent spatial SSH anomalies after removal of the first-order two-dimensional background. Red arrows highlight representative orientations of elongated SSH anomaly structures observed at Cherbourg and Étretat and illustrate their spatial variation in orientation across the respective domains. The red arrows are provided as visual guides to the geometry of the observed structures and do not represent wave or current propagation vectors. No clear preferential orientation was identified at Villers-sur-Mer.

3.4. Spatial Anomalies and σ^0 Correspondence

To examine whether the spatial variability identified in the detrended SSH fields is associated with variations in radar backscatter, co-located SSH anomalies and σ^0 observations were compared at the 50 m grid scale (Figure 8). The σ^0 fields exhibit marked

spatial variability across the three study sites, with distinct spatial distributions between Villers-sur-Mer, Étretat, and Cherbourg. In particular, the spatial organization and range of σ^0 differ substantially among the domains, indicating contrasting radar backscatter conditions during the selected acquisitions. Despite this pronounced spatial variability in σ^0, no meaningful point-by-point linear correspondence with the SSH spatial anomalies is observed. At Villers-sur-Mer, the correlation is negligible ($r = 0.004$, $N = 39.332$), while an essentially null correlation is also obtained at Étretat ($r = -0.001$, $N = 39.892$). Cherbourg similarly exhibits only a very weak negative correlation ($r = -0.036$, $N = 37.710$). The near-horizontal regression relationships and broad scatter of σ^0 values for comparable SSH anomalies further demonstrate the absence of a systematic linear dependence at the grid-cell scale.

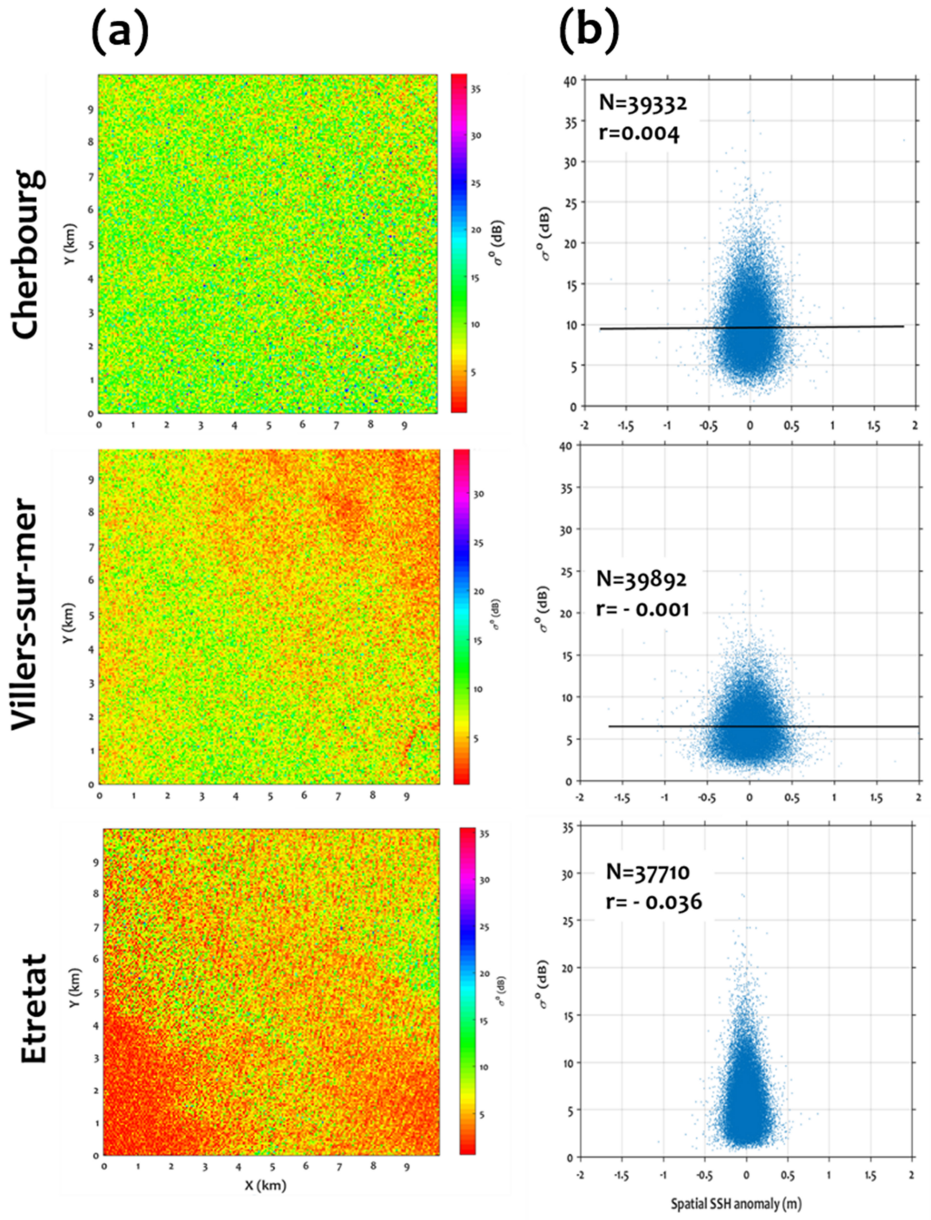


Figure 8. Spatial distribution of SWOT HR radar backscatter (σ^0) and its relationship with detrended SSH anomalies at Villers-sur-Mer, Étretat, and Cherbourg (from top to bottom). Column (**a**) shows the spatial distribution of σ^0 (dB), while column (**b**) presents the corresponding scatterplots between detrended SSH anomalies and σ^0. Pearson correlation coefficients (r) and numbers of valid collocated grid cells (N) are indicated. Black lines represent linear regression fits.

These results indicate that the fine-scale SSH structures identified after detrending cannot be explained as a simple linear response to local variations in radar backscatter. At the same time, the pronounced and spatially structured σ^0 variability provides complementary information on differences in surface-state and radar-scattering conditions among the three domains. The physical significance of this spatial variability and its relationship with the observed SSH structures are considered further in the Discussion.

3.5. Scale-Dependent Organization of Storm-Time SSH Variability

3.5.1. Dominant Spatial Scales of SSH Variability

The detrended anomaly fields demonstrate that substantial spatial variability persists after removal of the broad-scale background, but they do not directly quantify the characteristic spatial scales associated with these structures. A two-dimensional Morlet wavelet analysis was therefore applied to the detrended SWOT HR SSH fields to resolve the distribution of variability across spatial scales while preserving its spatial localization.

The global 2-D Morlet wavelet spectra reveal a broad distribution of storm-time SSH variability across spatial scales, with substantial power concentrated at sub-kilometer to kilometer wavelengths (Figure 9). Across the three domains, wavelet power increases rapidly from the shortest investigated wavelengths and develops broad maxima within approximately 0.5–1.0 km, indicating that a substantial component of the residual HR variability is organized within this scale range.

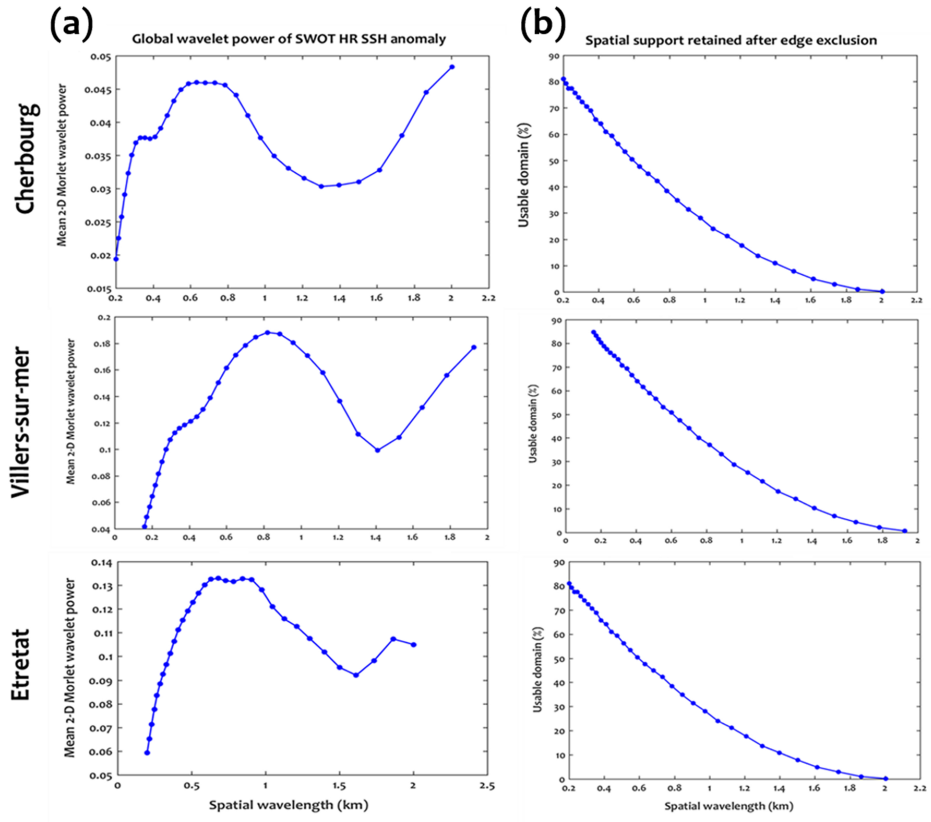


Figure 9. Global two-dimensional Morlet wavelet spectra of the detrended SWOT HR SSH fields (**a**) and corresponding spatial support retained after edge exclusion (**b**) for Cherbourg (**upper panels**), Villers-sur-Mer (**middle panels**), and Étretat (**lower panels**). The global spectra represent the mean 2-D Morlet wavelet power as a function of spatial wavelength. The right panels indicate the fraction of the analysis domain remaining usable at each wavelength after exclusion of edge-affected regions.

At Cherbourg, wavelet power increases rapidly from approximately 0.2 km and develops a broad elevated band between approximately 0.5 and 0.8 km, before decreasing toward wavelengths of approximately 1.2–1.5 km. At Villers-sur-Mer, the spectral maximum is shifted toward slightly larger spatial scales, with the highest power occurring around 0.8–0.9 km. At Étretat, elevated wavelet power extends across a relatively broad band between approximately 0.6 and 0.9 km, followed by a progressive decrease toward larger wavelengths. Despite these differences, the three domains therefore share a recurrent energetic scale range of approximately 0.5–1.0 km, while the position and breadth of the spectral maxima remain site dependent.

An accurate interpretation of the largest wavelengths requires greater caution because the spatial support available to the wavelet analysis decreases progressively with increasing scale (Figure 9b). The fraction of the domain retained after edge exclusion decreases substantially toward longer wavelengths. Although renewed increases in wavelet power are visible toward approximately 1.8–2.0 km, particularly at Cherbourg and Villers-sur-Mer, these features occur when only a small fraction of the original domain remains available for analysis. They therefore cannot be interpreted with the same confidence as the recurrent 0.5–1.0 km energetic band, which is identified while a considerably larger fraction of the spatial domain remains available after edge exclusion.

Overall, the wavelet spectra identify a recurrent energetic scale range of approximately 0.5–1.0 km across the three SWOT HR domains, superimposed on site-dependent differences in spectral organization. However, the global spectra quantify the relative importance of these scales at the domain level without indicating where the corresponding structures occur. Their spatial localization is therefore examined in the following section.

3.5.2. Scale–Space Organization of SSH Variability

The global wavelet spectra identify a recurrent energetic range of approximately 0.5–1.0 km across the three domains, but this domain-averaged representation does not indicate where the corresponding variability occurs within each 10 × 10 km field. To examine the spatial distribution of these energetic scales, wavelet power was represented jointly in X–Y–wavelength space (Figure 10). This scale–space representation preserves both the spatial localization and characteristic wavelength of elevated wavelet power, providing a three-dimensional view of the multiscale organization of the SSH anomalies.

The resulting distributions show that elevated wavelet power is not uniformly distributed across the domains. Instead, it occurs in spatially localized structures whose position, extent, and wavelength range vary among the three sites. Importantly, the recurrent ~0.5–1.0 km energetic range identified from the global spectra is expressed through multiple localized regions of enhanced power rather than as a spatially homogeneous signal.

At Cherbourg, elevated wavelet power is distributed across several spatially separated regions and extends over a relatively broad range of scales (Figure 10, upper panel). The strongest localized structures occur predominantly within the sub-kilometer range, with multiple regions of enhanced power between approximately 0.5 and 0.9 km. Their occurrence at different X–Y positions demonstrates that the energetic band identified in the global spectrum results from several spatially distinct structures rather than from a single feature.

At Villers-sur-Mer (Figure 10, middle panel), elevated wavelet power is more spatially concentrated, with the strongest structures occurring predominantly within the approximately 0.6–0.9 km range. Several vertically aligned concentrations of power extend across neighboring wavelength levels, indicating that variability at different scales can coexist within restricted portions of the domain. Shorter-scale structures are more widely distributed but generally exhibit lower power.

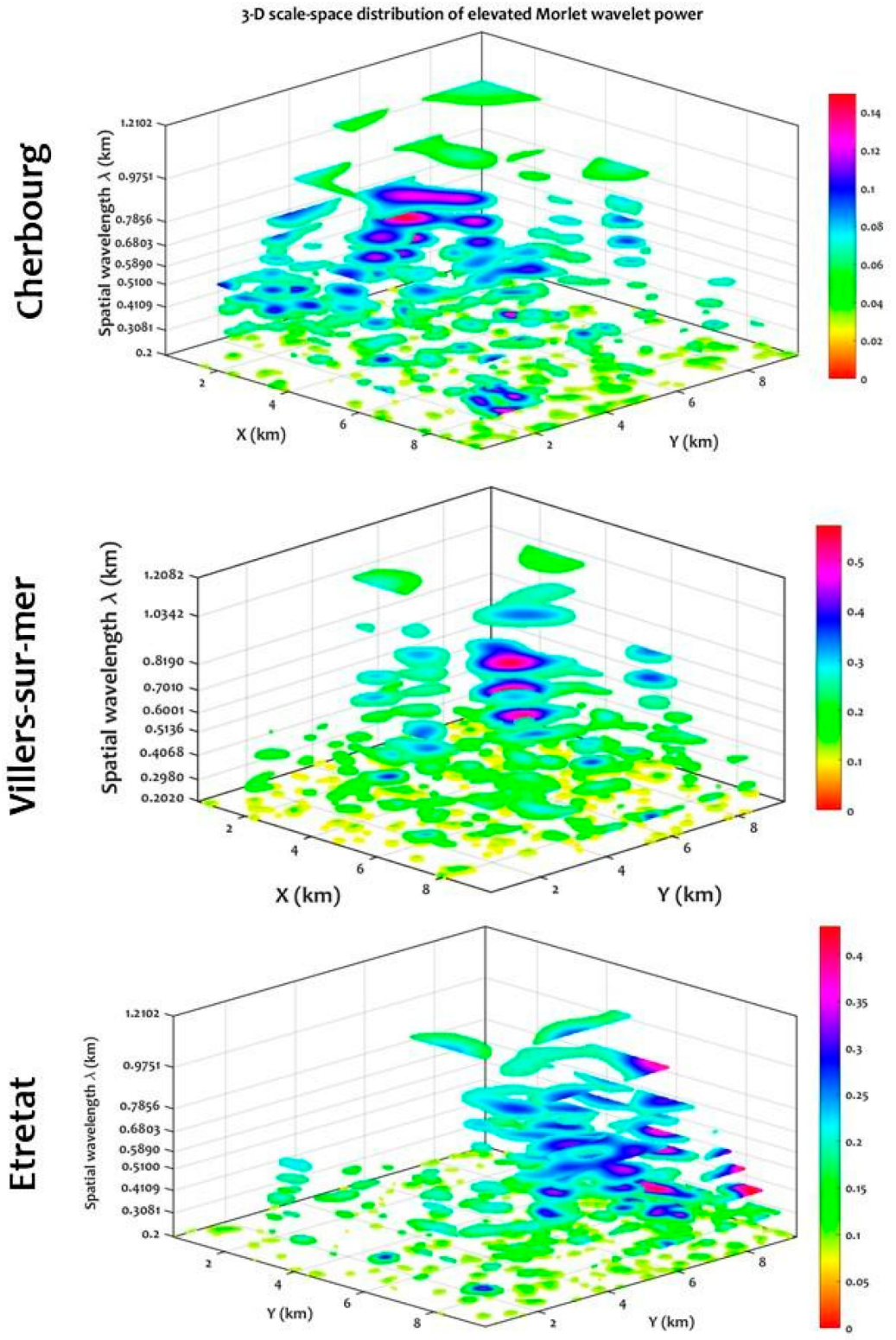


Figure 10. Three-dimensional scale–space distribution of elevated 2-D Morlet wavelet power for the detrended SWOT HR SSH fields at Cherbourg (**upper panel**), Villers-sur-Mer (**middle panel**), and Étretat (**lower panel**). The horizontal axes represent spatial position within each 10 × 10 km domain, while the vertical axis represents spatial wavelength. Colors indicate wavelet-power magnitude. Only elevated wavelet-power regions are represented to highlight the spatial localization and multiscale organization of the SSH variability.

At Étretat (Figure 10, lower panel), the scale–space organization differs markedly, with a pronounced concentration of elevated power within one part of the domain. This localized

energetic region extends across several neighboring wavelength levels, approximately from 0.4 to 0.9 km, indicating a locally multiscale organization of the SSH variability. Outside this principal region, the wavelet power is generally weaker and more spatially fragmented.

Taken together, these results demonstrate the capacity of SWOT HR to resolve not only storm-time coastal water-level variability, but also its two-dimensional multiscale organization, revealing spatially localized structures from sub-kilometer to kilometer scales.

3.5.3. Spatial Evolution of Wavelet Power Across Wavelengths

The scale–space representation demonstrates that enhanced wavelet power is spatially localized and distributed across multiple wavelengths. To further examine how this spatial organization evolves with scale, wavelet-power maps were extracted at successive representative wavelengths (Figures 11–13). This wavelength-resolved representation complements the global spectra and three-dimensional scale–space analysis by showing whether regions of enhanced power persist across neighboring scales, shift spatially within the domain, or reorganize as wavelength increases.

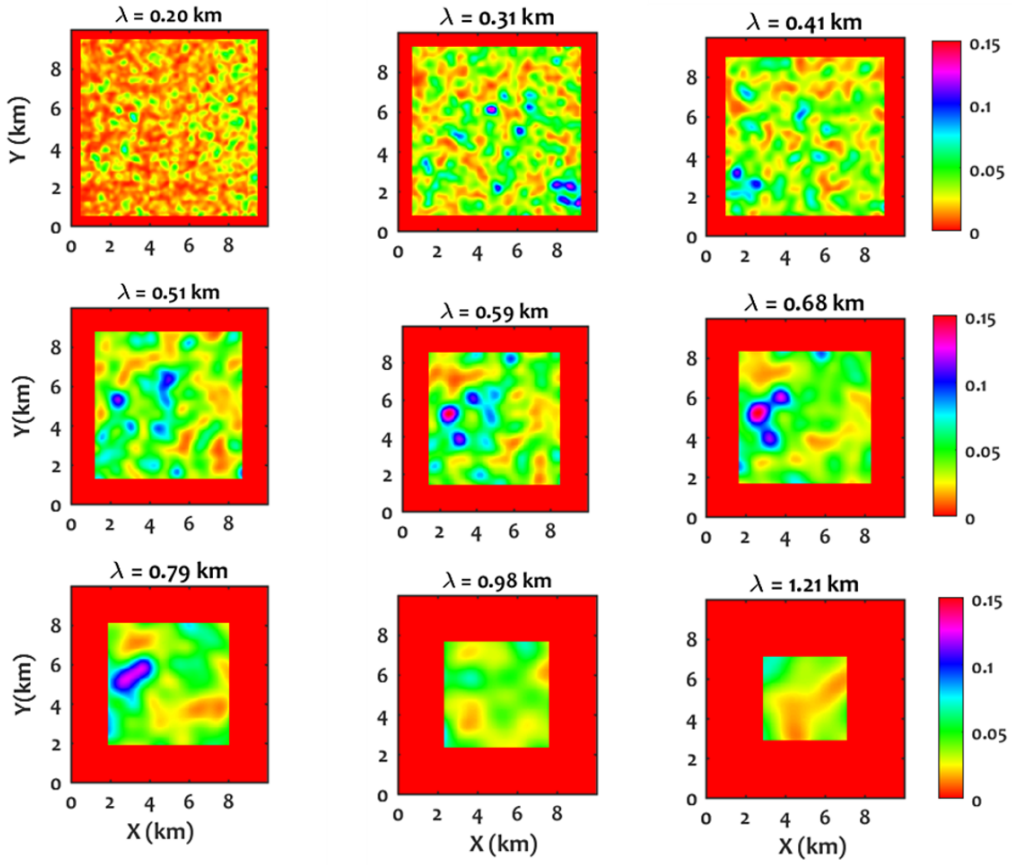


Figure 11. Spatial distribution of Morlet wavelet power across selected wavelengths derived from the detrended SWOT HR SSH anomaly at Cherbourg. Two-dimensional wavelet-power maps are shown for spatial wavelengths ranging from 0.20 to 1.21 km. Red regions indicate areas excluded from the analysis because of edge effects, with the valid spatial domain progressively decreasing toward longer wavelengths. The sequence illustrates the transition from relatively fine-scale, spatially distributed variability at short wavelengths to larger and more spatially coherent structures at intermediate wavelengths.

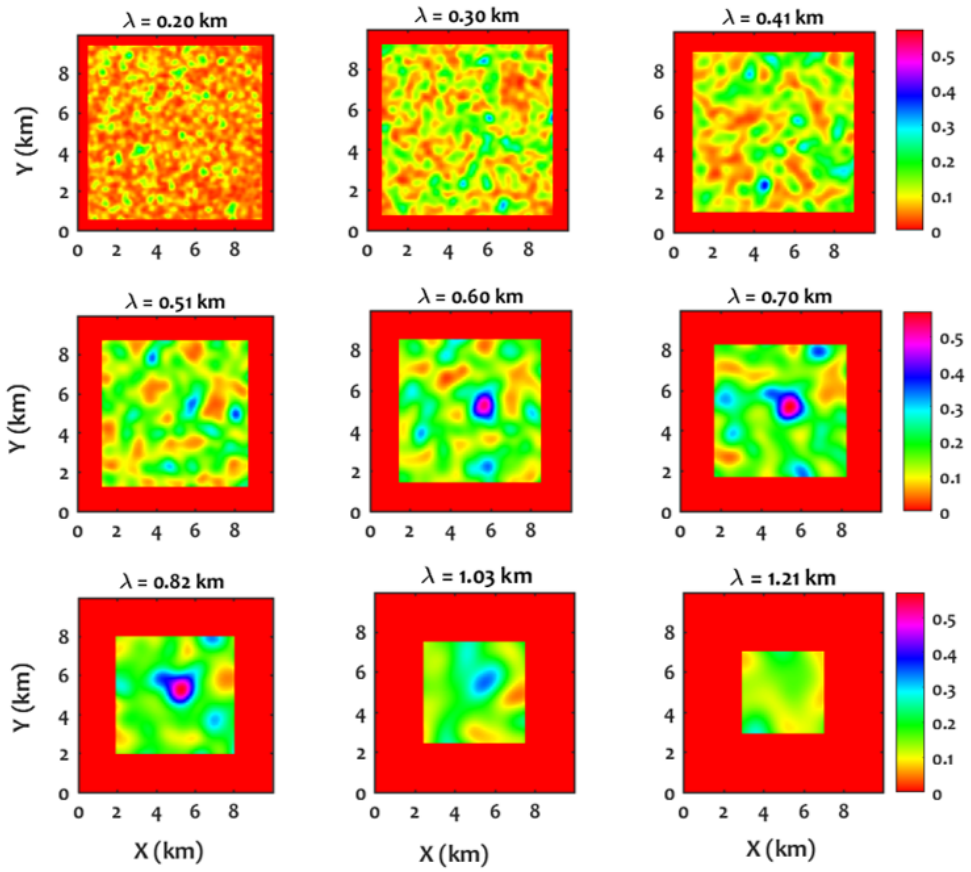


Figure 12. Spatial distribution of Morlet wavelet power across selected wavelengths derived from the detrended SWOT HR SSH anomaly at Villers-sur-mer. Two-dimensional wavelet-power maps are shown for spatial wavelengths ranging from 0.20 to 1.21 km. Red regions indicate areas excluded from the analysis because of edge effects, with the valid spatial domain progressively decreasing toward longer wavelengths. The sequence illustrates the transition from relatively fine-scale, spatially distributed variability at short wavelengths to larger and more spatially coherent structures at intermediate wavelengths.

At Cherbourg, the wavelength-resolved maps reveal a progressive reorganization of wavelet power across scales (Figure 11). At the shortest investigated wavelengths (λ = 0.20–0.31 km), elevated power is distributed among numerous small and spatially fragmented regions across much of the usable domain. At $\lambda \approx$ 0.41–0.51 km, the distribution becomes less fragmented, with distinct regions of enhanced power progressively emerging within the field. This organization becomes particularly pronounced within the energetic range identified from the global spectrum. Between approximately 0.59 and 0.79 km, enhanced power is concentrated within fewer localized regions, several of which persist across successive wavelength levels. This persistence indicates that the broad energetic band identified at Cherbourg is associated with spatially organized multiscale structures rather than with a spatially uniform increase in variability. At $\lambda \approx$ 0.98–1.21 km, broader regions of enhanced power remain visible, although the progressive reduction in the usable domain due to edge exclusion limits their spatial interpretation.

At Etretat a similar transition from fragmented short-scale variability toward localized intermediate-scale structures is observed (Figure 13). At λ = 0.20–0.31 km, elevated power is distributed among numerous small structures throughout the domain. At $\lambda \approx$ 0.41–0.51 km, distinct regions of enhanced power progressively emerge while the overall spatial distribution becomes less fragmented. Within the energetic range identified from the global spectrum, particularly between approximately 0.59 and 0.79 km, wavelet power becomes

concentrated within a restricted portion of the domain. A pronounced energetic region around X ≈ 2–4 km and Y ≈ 4–6 km persists across successive wavelength levels, demonstrating that the spectral maximum observed at Villers-sur-Mer is associated with a spatially localized multiscale structure rather than with uniformly distributed variability. At λ ≈ 0.98 km, the spatial distribution of the strongest power changes while the usable domain becomes substantially reduced, and interpretation at λ = 1.21 km is further constrained by edge exclusion.

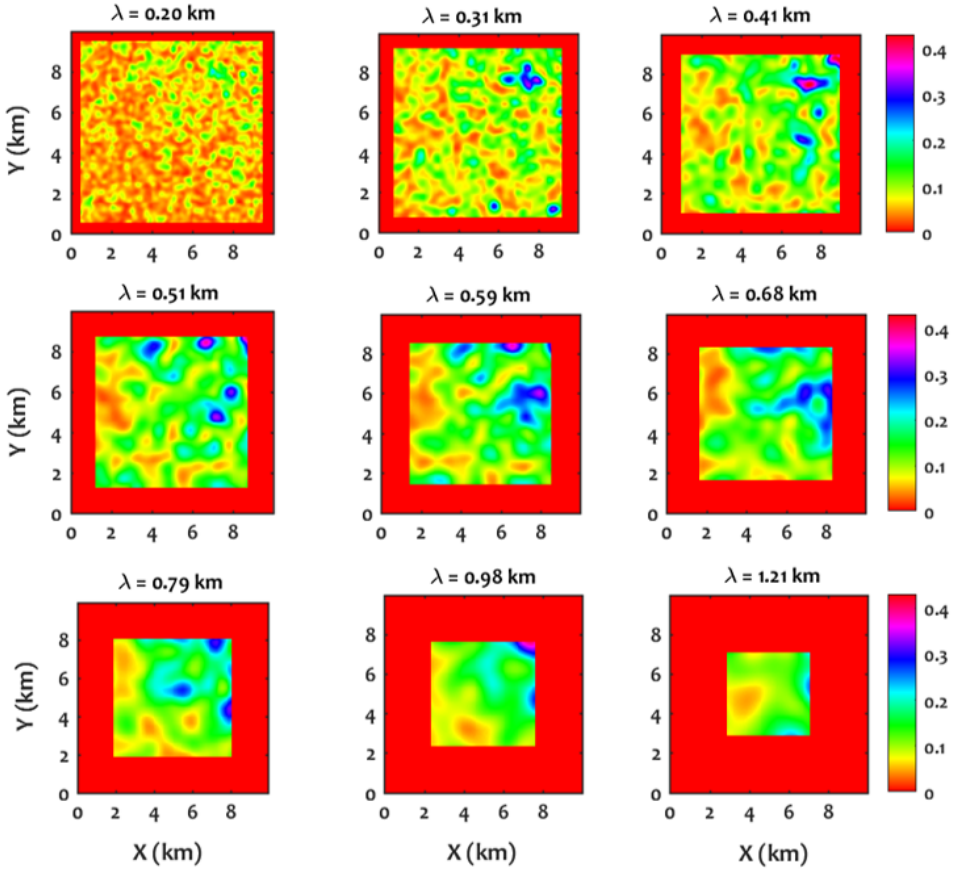


Figure 13. Spatial distribution of Morlet wavelet power across selected wavelengths derived from the detrended SWOT HR SSH anomaly at Etretat. Two-dimensional wavelet-power maps are shown for spatial wavelengths ranging from 0.20 to 1.21 km. Red regions indicate areas excluded from the analysis because of edge effects, with the valid spatial domain progressively decreasing toward longer wavelengths. The sequence illustrates the transition from relatively fine-scale, spatially distributed variability at short wavelengths to larger and more spatially coherent structures at intermediate wavelengths.

At Villers-sur-Mer, the wavelength-resolved maps show an equally clear but spatially distinct evolution (Figure 12). At λ = 0.20–0.30 km, wavelet power is distributed among numerous small structures throughout the domain. At λ ≈ 0.41–0.51 km, the distribution becomes less fragmented and several localized regions of enhanced power emerge. Between approximately 0.60 and 0.82 km, a pronounced concentration of wavelet power develops within the central part of the domain and persists across successive wavelength levels. The persistence and strengthening of this localized structure across neighboring scales are consistent with the broad energetic range identified in the global spectrum and indicate that the corresponding spectral signal is associated with a spatially coherent multiscale region. At λ ≈ 1.03 km, broader variability remains visible within the reduced usable domain,

whereas at $\lambda = 1.21$ km the strong reduction in spatial support limits interpretation of the remaining structures.

Across the three domains, the wavelength-resolved maps therefore reveal a common transition from spatially fragmented variability at the shortest wavelengths toward more localized and persistent energetic structures within the ~0.5–1.0 km range. However, the spatial expression of this scale evolution differs among sites. Cherbourg exhibits several spatially separated energetic regions, whereas Villers-sur-Mer and Étretat show more concentrated regions of enhanced power that persist across neighboring wavelengths. These results confirm that the recurrent energetic range identified from the global spectra reflects spatially organized multiscale SSH variability, while its spatial footprint and persistence remain strongly site dependent.

3.5.4. Localization of Enhanced Scale-Dependent Variability

The wavelength-resolved analysis demonstrates that regions of enhanced wavelet power evolve spatially across scales and may persist over several neighboring wavelengths. To identify the portions of each domain where this scale-dependent variability is preferentially concentrated, wavelet power was integrated over the 0.5–0.8 km wavelength band, corresponding to the core of the recurrent energetic range identified across the three domains and remaining sufficiently supported by the CWT analysis. This scale-integrated representation provides a spatial synthesis of the distribution of enhanced wavelet power within the selected wavelength band, complementing the analysis at individual wavelengths (Figure 14).

The scale-integrated maps reveal that variability within the 0.5–0.8 km band is strongly heterogeneous and spatially localized (Figure 14). Overall, enhanced wavelet power is more pronounced and spatially extensive at Villers-sur-Mer and Étretat than at Cherbourg, with distinct spatial organizations between the two sites. At Cherbourg, several distinct regions of enhanced power are evident, with the strongest maxima clustered mainly within the left-central portion of the retained domain and additional localized maxima occurring elsewhere. At Villers-sur-Mer, the organization differs markedly, with a pronounced maximum near the central part of the domain accompanied by several secondary regions of enhanced power. At Étretat, the integrated power exhibits a more asymmetric spatial distribution, with enhanced variability preferentially expressed across the central-to-right part of the retained domain and several localized maxima toward its upper and right-hand portions. These contrasting patterns demonstrate that the recurrent energetic wavelength range identified across the three sites does not correspond to a spatially homogeneous response.

Figure 14 therefore provides a spatial synthesis of the scale-dependent behavior identified in the preceding analyses. Whereas the global spectra establish the recurrence of energetic wavelengths, the scale–space representation and wavelength-resolved maps describe their spatial localization and evolution across individual scales. Integration over the 0.5–0.8 km band identifies the preferential locations where enhanced variability is concentrated within the selected wavelength band. The three domains thus share a comparable energetic scale range while exhibiting markedly different spatial distributions of wavelet power.

Based on these results, the wavelet analyses provide complementary evidence for the multiscale organization of storm-time SWOT HR SSH variability. The global spectra identify a recurrent energetic range of approximately 0.5–1.0 km; the scale–space analysis demonstrates that this variability is spatially localized; the wavelength-resolved maps reveal its evolution and persistence across neighboring scales; and the scale-integrated maps identify the preferential locations of enhanced variability within the core 0.5–0.8 km

band. The recurrent energetic range is therefore a common feature across the three domains, while its spatial expression remains localized and strongly site dependent.

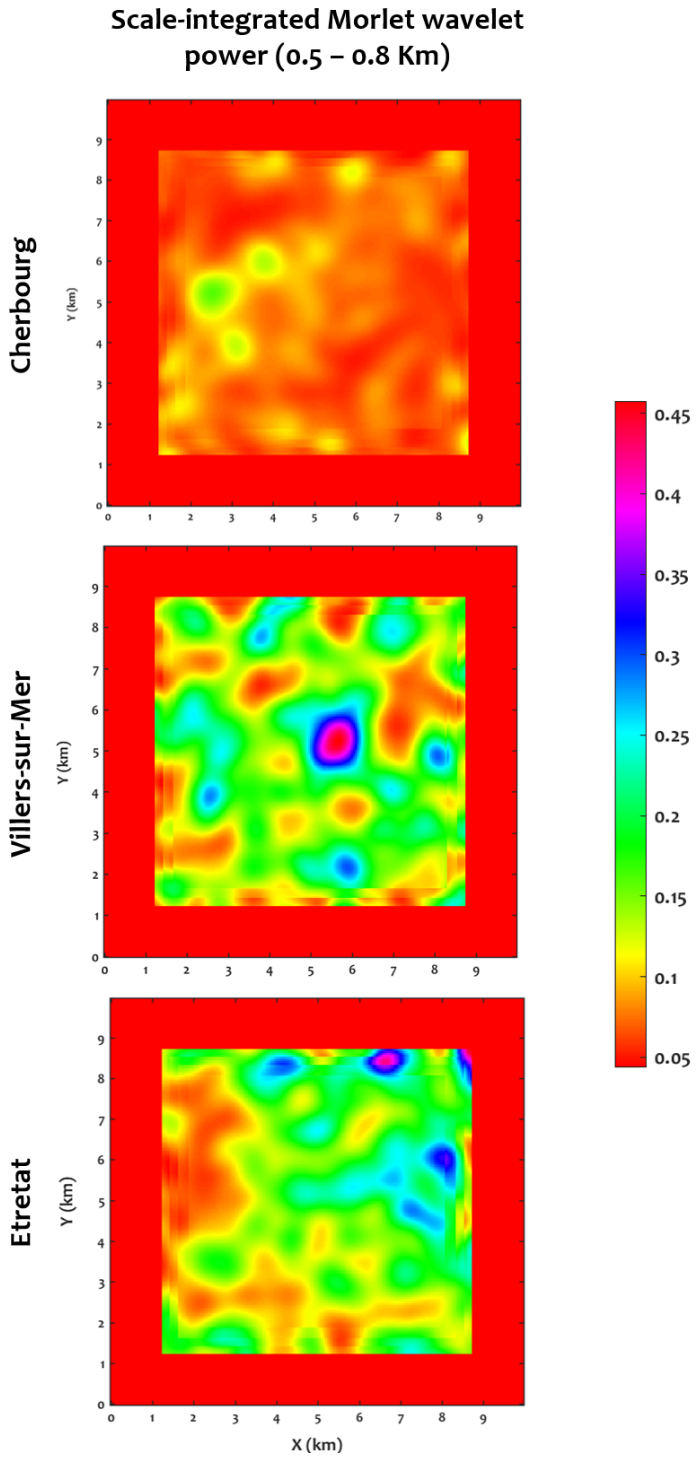


Figure 14. Spatial distribution of scale-integrated Morlet wavelet power within the 0.5–0.8 km wavelength band at Cherbourg, Villers-sur-Mer, and Étretat. Wavelet power was integrated over the common 0.5–0.8 km spatial-wavelength range identified within the energetic and sufficiently supported portion of the CWT spectra. The maps highlight the spatial localization of sub-kilometer SSH variability observed by SWOT HR and reveal contrasting patterns among the three coastal sites. Red areas correspond to regions excluded because of edge effects.

4. Discussion

4.1. Added Value of SWOT HR for Characterizing Fine-Scale Coastal SSH Variability

The present results demonstrate that SWOT HR observations can reproduce coastal water-level variability with high accuracy, while also revealing a pronounced spatial dependence in retrieval performance. The strongest agreement with tide-gauge observations was obtained at Cherbourg and Le Havre, where RMSE values are approximately 0.11 m, correlation coefficients exceed 0.99, biases are negligible, and regression slopes remain close to unity. Good agreement is also obtained at Saint-Malo and Diélette, although with greater dispersion. In contrast, the substantially larger errors observed at Dieppe demonstrate that SWOT HR performance cannot be adequately represented by a single accuracy estimate across heterogeneous coastal environments.

These results extend previous assessments of SWOT water levels in the English Channel. Turki et al. [29] evaluated coastal water levels using the SWOT L2 Expert product, demonstrating the capability of SWOT to reproduce water-level variability across this highly dynamic regional environment. The present study builds upon this regional assessment by exploiting HR PIXC observations, shifting the focus from coastal water-level validation toward the characterization of fine-scale two-dimensional SSH organization during storm conditions. This distinction is important because the PIXC observations retain substantially finer spatial information, which is required here to investigate localized SSH anomalies, their geometry, and their characteristic spatial scales.

The accuracy obtained at the best-performing sites is also consistent with the growing evidence that SWOT can provide reliable water-level observations in complex coastal and estuarine environments. In the hyper-tidal Bristol Channel–Severn Estuary, for example, Lichtman et al. [26] reported RMSDs ranging from 0.059 to 0.150 m against individual water-level gauges after accounting for spatially dependent offsets, with an overall RMSD of 0.137 m and a regression slope of 0.99. The approximately 0.11 m RMSE obtained here at Cherbourg and Le Havre therefore lies within the range of accuracy reported in recent coastal SWOT assessments. Direct numerical comparison should nevertheless remain cautious because the SWOT products, spatial aggregation, reference observations, environmental settings, and validation strategies differ among studies.

The strong site dependence identified here is equally significant. Coastal validation inherently compares a spatially distributed satellite observation with a point measurement, and the correspondence between the two may be influenced by their spatial separation, local water-level gradients, coastal geometry, bathymetry, intertidal environments, and the distribution and quality of valid SWOT observations. Previous observations in highly dynamic coastal-estuarine environments have similarly shown that spatial differences between SWOT observations and gauge locations can introduce systematic differences, with coastal dynamics, hydrology, and morphology further influencing satellite–gauge comparisons [26]. These considerations support interpreting the poorer performance observed at Dieppe as a site-dependent limitation requiring specific investigation, rather than as representative of SWOT HR performance throughout the English Channel.

The relevance of spatial sampling has also been highlighted by studies exploiting high-resolution SWOT observations in complex coastal environments. Hart-Davis et al. [35] demonstrated the potential of SWOT products, including fine-scale PIXC observations, to characterize coastal water-level variability and highlighted the importance of local coastal configuration and observational sampling when interpreting high-resolution SWOT measurements. In this context, the 50 m grid adopted in the present study provides a common spatial framework for exploiting the dense PIXC observations and performing the subsequent two-dimensional analyses. Importantly, however, this 50 m spacing represents the sampling interval of the analysis grid and not the effective independent spatial resolution

of KaRIn. This distinction is essential when interpreting the finest structures represented in the gridded HR fields.

Beyond point-scale accuracy, the present results also emphasize an important advantage of SWOT: its capacity to observe the two-dimensional spatial organization of coastal water levels. This capability has recently been demonstrated for storm conditions by Vega-Gimenez et al. [30], who used both the SWOT L3 2 km and 250 m unsmoothed products to investigate the spatial footprint of storm surges across contrasting coastal environments. Their analysis showed that SWOT can provide two-dimensional information on storm-driven sea-level variability that cannot be obtained from individual tide gauges alone. This represents an important conceptual transition from conventional point-based validation toward the exploitation of SWOT as a spatial observing system for coastal dynamics.

To further assess whether the spatial organization identified from the HR PIXC observations is also detectable in a more aggregated SWOT product, the 250 m unsmoothed product was examined over the Cherbourg domain (Figure 15). The WSE (SSH+ cross-correction) derived from SSH_karin reproduces the broad spatial organization observed in the HR field (Figure 15a). More importantly, after removal of a first-order two-dimensional spatial background, the ssha_karin_2 field retains a clearly structured spatial anomaly pattern (Figure 15b). Because the LR fields were neither interpolated nor smoothed in this study, this agreement indicates that the kilometer-scale structures in the HR fields are not artifacts of the 50 m gridding. The comparison does not, however, constitute independent validation. Both products derive from the same KaRIn acquisition and therefore share instrument and processing errors. In addition, structures shorter than about 500 m cannot be resolved at 250 m posting.

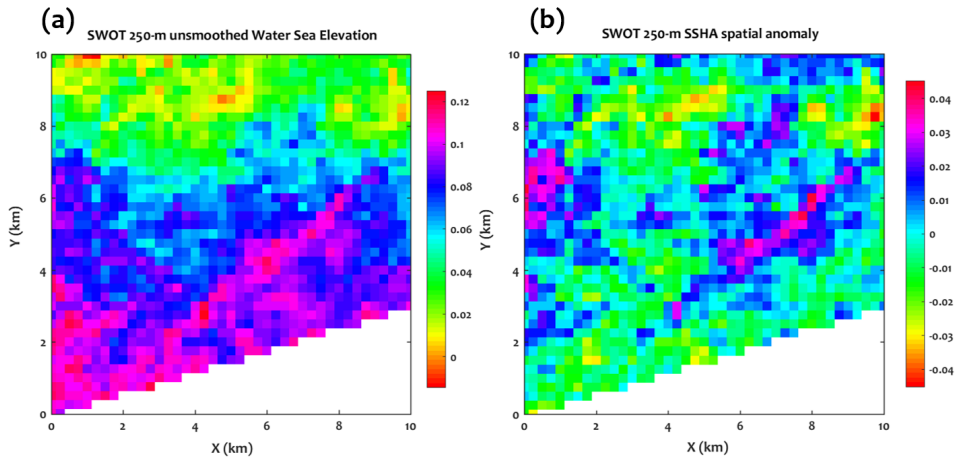


Figure 15. Spatial variability of the SWOT 250 m unsmoothed product over the Cherbourg study domain. (**a**) Water surface elevation (WSE) from the wse_karin_2 variable. (**b**) Spatial sea surface height anomaly (SSHA) obtained from ssha_karin_2 after removal of a first-order two-dimensional spatial background. White areas indicate locations without valid observations. No spatial interpolation or smoothing was applied.

Nevertheless, the comparison also illustrates the specific advantage of HR PIXC for the objectives of the present study. The 250 m unsmoothed product resolves the broad geometry and organization of the residual SSH variability, but its coarser spatial sampling provides substantially fewer observations across individual structures. The HR PIXC representation therefore does not reveal an entirely different spatial signal; rather, it provides a denser description of the same underlying organization and retains finer spatial variability that is less clearly represented at 250 m. This additional spatial information is particularly important for characterizing the geometry and orientation of the SSH anomalies and for

resolving their scale-dependent organization through the subsequent wavelet analysis. This comparison is consistent with the growing use of the SWOT 250 m unsmoothed product for investigating two-dimensional coastal and storm-related sea-level variability. In particular, Vega-Gimenez et al. [30] demonstrated the capability of the Unsmoothed 250 m SWOT_L3_LR_SSH product to characterize the spatial footprint of storm-driven sea-level anomalies across contrasting coastal environments from the Baltic, North Sea, and Gulf of Mexico, spanning micro-to macro-tidal contexts. The present comparison extends this perspective by showing that, at Cherbourg, the broad spatial organization evident at 250 m persists when moving to HR PIXC, while the latter provides the spatial sampling required to investigate the internal sub-kilometer-to-kilometer organization of these structures. Together with the tide-gauge validation, this cross-product consistency provides confidence for interpreting the spatial organization identified in the HR observations, while emphasizing that its detailed expression remains dependent on the local coastal environment.

The interpretation of fine-scale SSH variability also requires consideration of potential observational and processing uncertainties. KaRIn measurement noise, sea-state related retrieval effects, coastal contamination, residual tidal variability, and gridding as well as the filling gaps procedures contribute to the observed SSH anomalies. The comparison with the 250 m unsmoothed product at Cherbourg suggests that the broader spatial organization is not solely introduced by the 50 m PIXC gridding procedure. However, this comparison does not independently establish the geophysical origin of the sub-kilometer structures or exclude spatially correlated measurement errors. Similarly, removing a first-order spatial background does not eliminate residual tidal variability or structured measurement errors, while the weak linear relationship between SSH anomalies and radar backscatter does not exclude more complex retrieval effects. The identified ~0.5–1.0 km energetic scale range should therefore be interpreted as a characteristic of the processed SWOT HR fields, whose physical origin and sensitivity to observational uncertainties require further investigation.

4.2. Physical Drivers of Storm-Time SSH Spatial Variability

The enhanced SSH variability observed at spatial scales of approximately 0.5–1.0 km across the three study sites raises questions about the physical processes involved. During storms, coastal sea surface height is influenced by several interacting processes, including tides, storm surges, waves, currents, and local bathymetry. The spatial patterns observed by SWOT HR may therefore reflect the combined effects of these processes rather than a single physical mechanism.

One interesting result is the presence of enhanced wavelet power within the ~0.5–1.0 km range at all three sites. These scales are comparable to those reported in previous SWOT studies of long surface waves. For example, Ardhuin et al. [31] showed that SWOT can resolve long swells and their changes during propagation, including effects related to currents, refraction, diffraction, and coastal reflection. This similarity suggests that wave-related processes may contribute to the SSH variability observed in our study. However, the spatial scales identified by the wavelet analysis do not necessarily correspond directly to individual wave wavelengths. The identified spatial scales could be associated with long-wave motions of comparable wavelengths or with larger spatial structures influenced by wave transformation, wave–current interactions, and other coastal processes.

The presence of a similar energetic scale range at the three sites is also interesting because their coastal environments are different. However, the location, intensity, and shape of the SSH structures vary considerably from one site to another. This suggests that local conditions may influence how storm-time SSH variability is distributed, even when enhanced variability occurs at comparable spatial scales.

To better understand these differences, we compared the bathymetry, surface currents, wave conditions, and water levels at the three sites during the SWOT acquisitions (Figure 16). These fields provide information about the local hydrodynamic and coastal environments. However, their spatial resolution is generally coarser than the scales identified by the wavelet analysis, particularly for the wave and current fields. They therefore help describe the conditions at each site but cannot directly explain the origin of the observed sub-kilometer SSH structures.

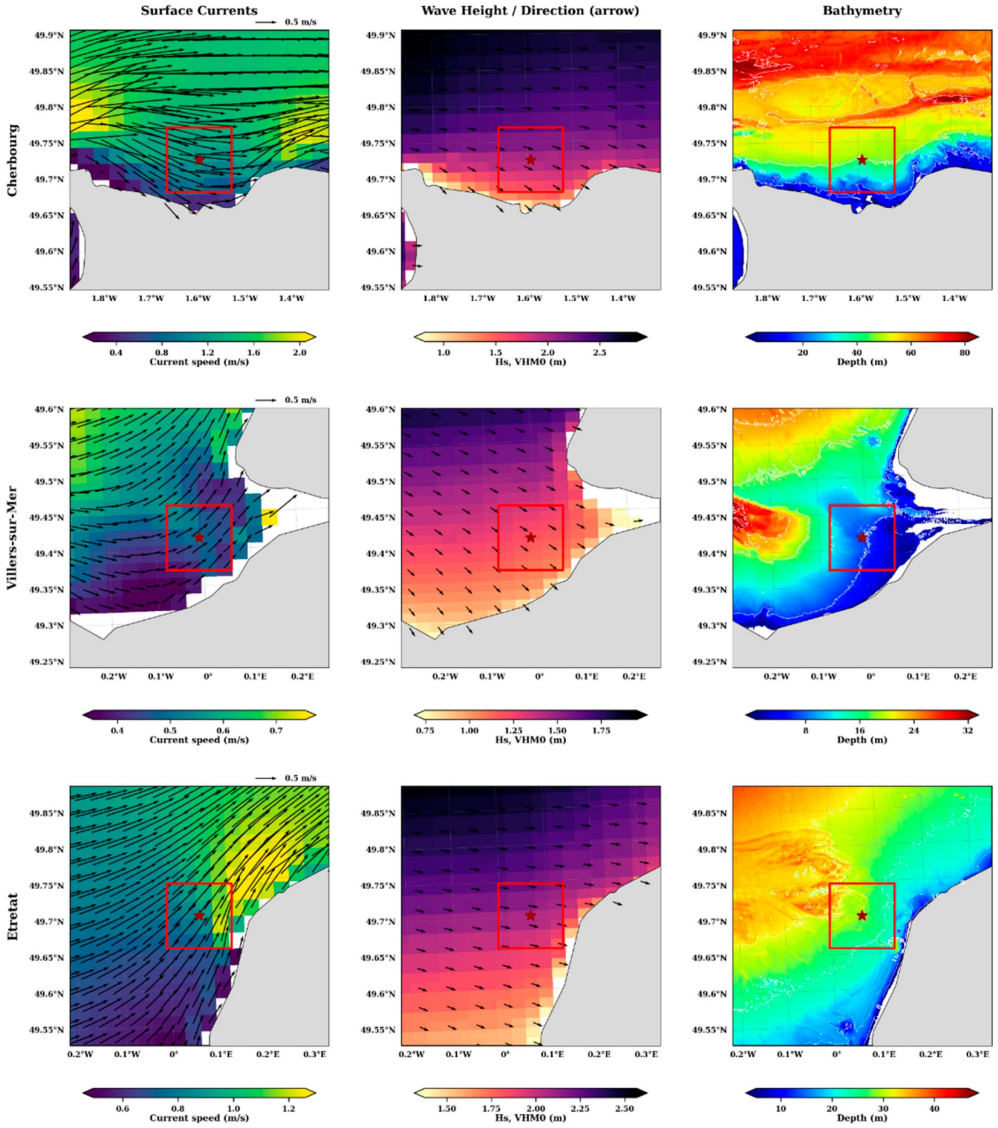


Figure 16. Bathymetry, modeled surface currents, wave conditions, and water levels during SWOT acquisitions at Cherbourg, Villers-sur-Mer, and Étretat. The 10 × 10 km SWOT HR study domains are indicated. The arrows indicate the direction of increasing distance along the transects, from 0 to 10 km. These environmental fields provide context for interpreting the observed spatial variability in SSH but do not allow the underlying physical processes responsible for the sub-kilometer SSH structures to be unambiguously identified.

The environmental fields show clear differences between the three sites (Figure 16). Cherbourg is characterized by relatively strong currents, marked bathymetric gradients, and energetic wave conditions. Villers-sur-Mer is shallower, with weaker currents, lower wave heights, and more complex nearshore bathymetry. Étretat also represents a coastal environment but differs from Villers-sur-Mer, with stronger currents, more energetic waves, and a pronounced cross-shore bathymetric gradient. These differences suggest that the

spatial organization of SSH variability may depend on several local factors, including bathymetry, waves, currents, and coastal geometry, rather than water depth alone.

Wave transformation is one possible process contributing to these patterns. As waves approach the coast, changes in water depth affect their speed, wavelength, and direction. Shoaling, refraction, diffraction, breaking, and interactions with currents can also modify the wave field. During storms, these processes occur together with tides, storm surges, and current-related water-level variations. Their combined effects may contribute to the complex SSH patterns observed by SWOT HR, although their individual roles cannot be determined from the present analysis.

Previous SWOT studies provide useful evidence of the mission's ability to observe wave-related processes. Ardhuin et al. [31] demonstrated that SWOT can detect long swells and their changes due to currents, refraction, diffraction, and coastal reflection. More recently, Islam et al. [33] used SWOT HR observations in the English Channel to investigate storm-generated swell transformation near the coast. Their results showed changes in wavelength with water depth, wave refraction, and diffraction around coastal obstacles. These findings were supported by comparisons with buoy measurements, theoretical relationships, and wave models. Although these studies focus on wave processes, they show that SWOT HR can resolve coastal wave structures at spatial scales comparable to those examined here.

Other studies have highlighted the ability of SWOT to capture spatial differences in wave conditions. Villas Bôas et al. [36] showed that KaRIn can resolve kilometer-scale changes in significant wave height in different ocean environments, including regions affected by strong currents and tropical cyclones. Their results also highlighted the role of current-induced refraction in shaping wave fields. Similarly, Ho et al. [28] demonstrated that SWOT can resolve spatial variations in significant wave height over scales of 10–90 km off Central California. Although these scales are larger than those considered in our study, these findings show the value of SWOT for observing the spatial variability of energetic wave fields.

The σ^0 observations provide further information about the spatial patterns. Although radar backscatter varies considerably across the three sites, the correlations between detrended SSH anomalies and σ^0 are close to zero. This indicates that the SSH patterns are not directly related to local changes in radar backscatter through a simple linear relationship. However, this does not exclude more complex relationships between SSH, surface roughness, and radar measurements. The two variables describe different properties of the sea surface, and their spatial variations do not necessarily follow the same patterns.

Overall, the ~0.5–1.0 km energetic scale range identified in the three cases examined here is consistent with spatial scales at which SWOT has previously observed long-wave structures. Wave-related processes may therefore contribute to the observed SSH variability, either directly through long-wave motions or indirectly through wave transformation and interactions with currents and bathymetry. However, the wavelet analysis identifies the spatial scales and locations of enhanced SSH variability rather than the physical origin of individual structures. The main finding is that comparable energetic scales are observed across the three coastal sites, while their spatial organization differs considerably. Further observations and high-resolution modeling will be needed to determine which processes contribute most strongly to these patterns.

4.3. Cross-Site Influence of Coastal Configuration and Storm Conditions

The comparison between Villers-sur-Mer and Étretat is particularly informative because both domains were observed during the same storm, reducing differences associated with the large-scale meteorological forcing. Nevertheless, their SSH spatial patterns differ considerably. The environmental fields presented in Figure 16 show that, despite both

being relatively shallow coastal environments, the two sites have different hydrodynamic and bathymetric characteristics. Villers-sur-Mer is associated with weaker currents, lower wave heights, and more complex shallow nearshore bathymetry, whereas Étretat exhibits stronger currents, more energetic wave conditions, and a pronounced cross-shore bathymetric gradient. These contrasts suggest that water depth or proximity to the coastline alone may not fully explain the differences in SSH spatial organization.

The EOF analysis further highlights these differences. At Villers-sur-Mer, EOF1 accounts for only 24.7% of the variance, with 65.9% remaining beyond the first six modes, consistent with the heterogeneous anomaly field and strongly localized wavelet-power distribution. In contrast, Étretat exhibits a stronger leading mode, with EOF1 explaining 37.5% of the variance, together with locally oriented SSH anomalies and a different spatial distribution of wavelet power. These observations suggest that local coastal conditions may influence how storm-time SSH variability is spatially expressed, although their individual contributions cannot be determined from the present analysis.

Cherbourg provides a complementary comparison because it represents a more open and deeper coastal setting observed during a different storm event. Its leading EOF mode explains 37.8% of the variance, comparable to Étretat, while its anomaly field contains pronounced elongated and locally oriented structures. Enhanced wavelet power is distributed among several localized regions. The environmental fields indicate relatively strong currents, energetic wave conditions, and marked bathymetric gradients. However, similarities in EOF contributions or anomaly geometry between Cherbourg and Étretat do not necessarily imply that the same physical processes are responsible. Comparable spatial characteristics may arise under different combinations of storm forcing and local coastal conditions.

An important distinction therefore emerges between the energetic scale range and the spatial organization of SSH variability. Enhanced variability within the approximately 0.5–1.0 km range is identified in all three cases examined, but its location, intensity, and geometry differ substantially among sites. The scale-integrated wavelet analysis further shows that enhanced power within the 0.5–0.8 km band is more pronounced and spatially extensive at Villers-sur-Mer and Étretat than at Cherbourg, despite the contrasting spatial organization observed at the two sites. This suggests that comparable energetic scales can occur under contrasting coastal conditions, while their spatial expression remains site dependent. However, the limited number of sites and storm events does not allow us to determine whether this scale range is a more general feature of storm-time coastal SSH variability.

Overall, these comparisons highlight the importance of considering both storm conditions and local coastal configuration when interpreting SWOT HR observations. The identification of a comparable energetic scale range in the three investigated cases does not imply a common spatial response or a unique underlying physical mechanism. Rather, SWOT HR reveals differences in the two-dimensional organization of storm-time SSH that may reflect the combined influence of local hydrodynamic and bathymetric conditions.

4.4. Implications for Coastal Monitoring and Future SWOT HR Applications

The ability of SWOT HR observations to resolve the two-dimensional and multiscale organization of coastal SSH has important implications for coastal monitoring. Tide gauges provide highly accurate and temporally resolved water-level records but remain spatially discrete, whereas SWOT provides a complementary two-dimensional representation of the water surface. Recent applications have demonstrated this added value in complex coastal environments and during storms [26,30]. The present results extend this perspective by

showing that storm-time SSH contains localized spatial structures that cannot be represented by a single domain-averaged water level.

The recurrence of enhanced variability within the ~0.5–1.0 km range, together with its strongly site-dependent spatial expression, demonstrates the potential of SWOT HR to characterize not only the magnitude of coastal water-level variability, but also its spatial scales, geometry, localization, and organization.

The two-dimensional wavelet analysis identified enhanced SSH variability within an approximately 0.5–1.0 km energetic scale range in all three coastal domains examined, despite substantial differences in the spatial organization of this variability. However, these findings are based on three 10 × 10 km domains and two storm events and should not be interpreted as evidence that this scale range is universally characteristic of storm-time coastal SSH variability. Additional SWOT HR observations covering a broader range of storm conditions and coastal environments are required to assess the persistence and generality of this result.

SWOT HR should therefore be viewed as complementary to, rather than a replacement for, existing coastal observing systems. Conventional nadir altimetry provides long-term observations of sea-level variability but remains constrained by along-track sampling and increasing retrieval complexity toward the coast [15], while SAR and other high-resolution Earth-observation techniques provide detailed two-dimensional information on waves, currents, sea-surface roughness, and coastal dynamics [12]. In this observational landscape, the distinctive contribution of SWOT lies in combining direct altimetric measurements of water-surface elevation with wide-swath two-dimensional sampling [18,20]. Future multi-mission approaches combining SWOT HR with SAR, wave observations, and in situ measurements could therefore provide a more complete characterization of the processes underlying spatially heterogeneous coastal water levels.

This spatial information may be particularly relevant for coastal-hazard assessment, where tides, storm surges, waves, currents, and local coastal configuration interact to produce spatially heterogeneous responses. Recent studies have demonstrated the capability of SWOT to characterize the spatial footprint of storm-driven sea-level anomalies [30] and coastal transformations of storm-generated waves [33]. Spatially resolved HR observations could therefore complement conventional observing systems for investigating locally enhanced variability relevant to extreme water levels, wave setup, and flooding, although direct attribution to individual hazard processes requires coincident observations and process-based modeling.

A further perspective concerns coastal modeling and data assimilation. Model evaluation is often constrained by the limited spatial coverage of in situ observations, whereas SWOT provides two-dimensional information that can potentially constrain not only absolute SSH but also its spatial organization. Recent assimilation experiments have already demonstrated the value of SWOT observations for constraining high-resolution ocean models [37]. The scale-resolved diagnostics developed here could extend this approach by comparing observations and simulations in terms of the spatial scales, geometry, and localization of variability, thereby moving beyond pointwise water-level validation toward evaluation of the spatial organization of the simulated coastal state.

These capabilities are also relevant to emerging integrated coastal prediction and Digital Twin Ocean frameworks, in which observations, numerical models, data assimilation, and forecasting are dynamically connected. Recent developments in the western English Channel illustrate the potential of such observation–prediction frameworks. Combining SWOT HR with tide gauges, wave and current observations, bathymetry, complementary Earth-observation missions, and high-resolution coastal models could therefore provide valuable two-dimensional constraints for future integrated coastal prediction systems.

Several considerations should nevertheless be taken into account when extending these results. SWOT HR provides spatially detailed observations of coastal SSH, but its temporal sampling remains insufficient to continuously follow the rapid evolution of individual storm events. At fine spatial scales, interpretation should also distinguish the 50 m analysis-grid sampling from the effective spatial resolution of the observations and account for the specific characteristics of coastal PIXC measurements. These considerations define the framework within which their physical interpretation and extension to broader coastal applications should be considered. The present study therefore demonstrates the value of SWOT HR for characterizing the two-dimensional and multiscale organization of storm-time coastal SSH, while repeated observations across additional storms and coastal environments will be required to assess the generality of the identified pattern.

Future work should extend the analysis across additional SWOT passes and storm events encompassing contrasting atmospheric and oceanic forcing conditions, coastal configurations, and hydrodynamic regimes. Combining repeated HR observations with coincident wave, current, bathymetric, radar-backscatter, and in situ measurements, together with process-based coastal modeling, will be essential for determining the persistence and physical origin of the recurrent energetic scales identified here and assessing their potential value for model validation and data assimilation.

The principal contribution of SWOT HR to coastal monitoring therefore lies not simply in providing water-level observations at finer spatial sampling, but in revealing the two-dimensional, multiscale organization of coastal SSH under energetic conditions. This capability provides a new observational dimension for connecting satellite altimetry with coastal dynamics, hazards, modeling, and integrated prediction.

Future studies combining SWOT HR observations with high-frequency coastal measurements and wave-resolving models could investigate whether part of the observed kilometer-scale SSH variability is associated with infragravity waves and other long-wave processes.

5. Conclusions

This study demonstrates the capability of SWOT High-Resolution (HR) observations to characterize the two-dimensional spatial organization of coastal sea surface height during energetic storm conditions. Across three contrasting domains in the English Channel, Cherbourg, Villers-sur-Mer, and Étretat, tide-gauge comparisons first confirm the ability of SWOT HR to reproduce coastal water-level variability, while also highlighting site-dependent differences in retrieval performance. Beyond point-scale validation, the HR observations reveal a complex spatial organization of storm-time SSH. EOF decomposition and detrended anomaly fields show that substantial spatial variability persists beyond the dominant large-scale structures. Most importantly, the scale-resolved analysis identifies enhanced SSH variability within an approximately 0.5–1.0 km energetic scale range in all three cases examined. This variability is not spatially homogeneous but occurs through localized multiscale structures whose geometry, intensity, and spatial distribution differ markedly among sites.

The cross-site comparison reveals an important distinction between the energetic scale range identified in the investigated cases and its strongly site-dependent spatial expression. The spatial patterns of enhanced wavelet power are more pronounced at Villers-sur-Mer and Étretat than at Cherbourg, highlighting differences in the intensity and spatial organization of sub-kilometer SSH variability among the three coastal environments. The contrast between Villers-sur-Mer and Étretat, despite their observation during the same storm, suggests that water depth or proximity to the coast alone cannot account for the observed differences in spatial organization. Their contrasting wave conditions, current regimes, and bathymetric configurations provide a plausible environmental context for

these differences, although the individual contributions of these processes cannot be isolated from the present observations.

The principal contribution of SWOT HR therefore lies not simply in providing coastal water-level observations at finer spatial sampling, but in revealing where and at which spatial scales storm-time SSH variability is organized. This two-dimensional, multiscale perspective provides a new observational basis for investigating coastal dynamics and for improving the representation of spatially heterogeneous coastal processes in monitoring and modeling frameworks. Nevertheless, the present findings are based on three 10 × 10 km domains and two storm events. In addition, the influence of observational and processing uncertainties on the identified structures must be further assessed to distinguish geophysical signals from instrumental artifacts. Whether the ~0.5–1.0 km range of enhanced wavelet energy persists across a wider range of storm conditions and coastal settings remains to be established. This will require additional SWOT HR observations, combined with in situ measurements and process-based numerical modelling.

Author Contributions: Conceptualization, E.I.T. and M.S.I.; methodology, E.I.T., M.S.I. and C.L.S.; validation, E.I.T., M.S.I. and C.L.S.; formal analysis, E.I.T., M.S.I. and C.L.S.; investigation, E.I.T., M.S.I., C.L.S., M.B.A. and A.A.; resources, E.I.T., M.S.I. and C.L.S.; data curation, E.I.T., M.S.I. and C.L.S.; writing—original draft preparation, E.I.T., M.S.I., C.L.S., M.B.A. and A.A.; writing—review and editing, E.I.T., M.S.I., C.L.S., M.B.A. and A.A.; visualization, E.I.T., M.S.I., C.L.S., M.B.A. and A.A.; supervision, E.I.T.; project administration, E.I.T.; funding acquisition, E.I.T. All authors have read and agreed to the published version of the manuscript.

Funding: This research received no external funding.

Data Availability Statement: The details regarding where data supporting reported results are provided, including links to publicly archived datasets analyzed or generated during the study. No new data were created.

Acknowledgments: This work was supported by the French Space Agency (CNES, Centre National d'Études Spatiales) through the SWOT4COST program and by the CNRS EONES-SWOT project. The authors also acknowledge CNES for its scientific and technical support regarding the use and analysis of SWOT High-Resolution products. We gratefully acknowledge SHOM, the UK Met Office, and IFREMER for providing the water-level, wave, and current datasets used for validation and interpretation of the results.Additional support was provided by TRANSITION FRANCE 2030 ANR-23-EXES-0013.

Conflicts of Interest: The authors declare no conflicts of interest.

Appendix A. Implementation of the Two-Dimensional Morlet Wavelet Analysis

The two-dimensional continuous wavelet transform (2-D CWT) was applied to the detrended SWOT HR spatial SSH anomaly, $\eta'(x,y)$, on the common 50 m grid. The transform was computed using a two-dimensional Morlet wavelet, allowing the spatial variability of SSH to be resolved simultaneously in terms of characteristic scale and spatial localization. The complex wavelet coefficients were calculated as

$$W(x,y,s) = \iint \eta'(x',y')\psi s*(x'-x,\ y'-y)dx'dy'$$

where s is the wavelet scale and $\psi s*$ denotes the complex conjugate of the scaled Morlet wavelet. Wavelet scales were converted to equivalent spatial wavelengths, λ, using the scale-to-wavelength relationship associated with the selected Morlet formulation. The same scale discretization and wavelength range were applied to Cherbourg, Villers-sur-Mer,

and Étretat to ensure direct comparison among the three sites. Local wavelet power was defined as

$$P(x, y, \lambda) = | W(x, y, \lambda) |^2$$

and spatially averaged power was calculated over the valid portion of each domain to identify the dominant energetic wavelength ranges. Because the spatial support of the wavelet increases with wavelength, coefficients affected by domain boundaries were excluded using a wavelength-dependent edge criterion. The fraction of the domain remaining valid was evaluated at each wavelength and considered jointly with the spatially averaged wavelet power, particularly when interpreting the largest detected scales.

Finally, wavelet power was integrated over the principal energetic wavelength bands identified from the spectra to map the spatial concentration of scale-dependent SSH variability. These maps were used to compare the localization of characteristic structures among the three coastal sites. The detected wavelengths represent characteristic spatial scales of SSH variability and were subsequently interpreted using independent information on waves, surface currents, water levels, bathymetry, and coastal configuration.

References

1. Masselink, G.; Gehrels, R. (Eds.) *Coastal Environments and Global Change*; Wiley-Blackwell: Chichester, UK, 2015. [CrossRef]
2. Switzer, A.D. Coastal hazards: Storms and tsunamis. In *Coastal Environments and Global Change*; Masselink, G., Gehrels, R., Eds.; Wiley-Blackwell: Chichester, UK, 2015; pp. 104–127. [CrossRef]
3. Haigh, I.D.; Marcos, M.; Talke, S.A.; Woodworth, P.L.; Hunter, J.R.; Hague, B.S.; Arns, A.; Bradshaw, E.; Thompson, P. GESLA Version 3: A major update to the global higher-frequency sea-level dataset. *Geosci. Data J.* **2023**, *10*, 293–314. [CrossRef]
4. Turki, I.; Baulon, L.; Massei, N.; Laignel, B.; Costa, S.; Fournier, M.; Maquaire, O. A nonstationary analysis for investigating the multiscale variability of extreme surges: Case of the English Channel coasts. *Nat. Hazards Earth Syst. Sci.* **2020**, *20*, 3225–3243. [CrossRef]
5. Wu, G.; Shi, F.; Kirby, J.T.; Liang, B.; Shi, J. Modeling wave effects on storm surge and coastal inundation. *Coast. Eng.* **2018**, *140*, 371–382. [CrossRef]
6. Hibbert, A.; Bradshaw, E.; Pugh, J.; Williams, S.; Woodworth, P. Tide Gauges: From Single Hazard to Multi-Hazard Warning Systems. *Oceanography* **2022**, *34*, 82–83. [CrossRef]
7. Williams, J.; Horsburgh, K.J.; Williams, J.A.; Proctor, R.N.F. Tide and skew surge independence: New insights for flood risk. *Geophys. Res. Lett.* **2016**, *43*, 6410–6417. [CrossRef]
8. Han, G.; Ma, Z.; Chen, D.; deYoung, B.; Chen, N. Observing storm surges from space: Hurricane Igor off Newfoundland. *Sci. Rep.* **2012**, *2*, 1010. [CrossRef] [PubMed]
9. Han, G.; Ma, Z.; Chen, N.; Chen, N.; Yang, J.; Chen, D. Hurricane Isaac storm surges off Florida observed by Jason-1 and Jason-2 satellite altimeters. *Remote Sens. Environ.* **2017**, *198*, 244–253. [CrossRef]
10. Chen, N.; Han, G.; Yang, J.; Chen, D. Hurricane Sandy storm surges observed by HY-2A satellite altimetry and tide gauges. *J. Geophys. Res. Oceans* **2014**, *119*, 4542–4548. [CrossRef]
11. Ji, C.; Li, G.; Zhang, Y. Observing storm surges in China's coastal areas by integrating multi-source satellite altimeters. *Estuar. Coast. Shelf Sci.* **2019**, *225*, 106224. [CrossRef]
12. Laignel, B.; Vignudelli, S.; Almar, R.; Becker, M.; Bentamy, A.; Benveniste, J.; Birol, F.; Frappart, F.; Idier, D.; Salameh, E.; et al. Observation of the Coastal Areas, Estuaries and Deltas from Space. *Surv. Geophys.* **2023**, *44*, 1309–1356. [CrossRef]
13. Turki, E.I.; Salameh, E.; Lopez Solano, C.; Islam, M.S.; Domingues, M.; Aouf, L.; Gutierrez, D.; Carbonnière, A.; Frappart, F. Multi-Source Satellite Altimetry for Monitoring Storm Wave Footprints in the English Channel's Coastal Areas. *Remote Sens.* **2025**, *17*, 3262. [CrossRef]
14. Passaro, M.; Cipollini, P.; Vignudelli, S.; Quartly, G.D.; Snaith, H.M. ALES: A multi-mission adaptive subwaveform retracker for coastal and open ocean altimetry. *Remote Sens. Environ.* **2014**, *145*, 173–189. [CrossRef]
15. Vignudelli, S.; Birol, F.; Benveniste, J.; Fu, L.-L.; Picot, N.; Raynal, M.; Roinard, H. Satellite Altimetry Measurements of Sea Level in the Coastal Zone. *Surv. Geophys.* **2019**, *40*, 1319–1349. [CrossRef]
16. Abdalla, S.; Kolahchi, A.; Ablain, M.; Adusumilli, S.; Aich Bhowmick, S.; Alou-Font, E.; Amarouche, L.; Andersen, O.B.; Antich, H.; Aouf, L.; et al. Altimetry for the future: Building on 25 years of progress. *Adv. Space Res.* **2021**, *68*, 319–363. [CrossRef]
17. Fu, L.-L.; Alsdorf, D.; Morrow, R.; Rodriguez, E.; Mognard, N. *SWOT: The Surface Water and Ocean Topography Mission—Wide-Swath Altimetric Elevation on Earth*; JPL Publication 12-5; Jet Propulsion Laboratory: Pasadena, CA, USA, 2012.

18. Fu, L.-L.; Pavelsky, T.; Cretaux, J.-F.; Morrow, R.; Farrar, J.T.; Vaze, P.; Sengenes, P.; Vinogradova-Shiffer, N.; Sylvestre-Baron, A.; Picot, N.; et al. The Surface Water and Ocean Topography Mission: A breakthrough in radar remote sensing of the ocean and land surface water. *Geophys. Res. Lett.* **2024**, *51*, e2023GL107652. [CrossRef]
19. Morrow, R.; Fu, L.-L.; Ardhuin, F.; Benkiran, M.; Chapron, B.; Cosme, E.; d'Ovidio, F.; Farrar, J.T.; Gille, S.T.; Lapeyre, G.; et al. Global Observations of Fine-Scale Ocean Surface Topography with the Surface Water and Ocean Topography (SWOT) Mission. *Front. Mar. Sci.* **2019**, *6*, 232. [CrossRef]
20. Rodriguez, E.; Esteban-Fernandez, D.; Peral, E.; Chen, C.; De Bleser, J.-W.; Williams, B. Wide-Swath Altimetry: A Review. In *Satellite Altimetry over Oceans and Land Surfaces*; Stammer, D., Cazenave, A., Eds.; CRC Press: Boca Raton, FL, USA, 2017; pp. 71–112. [CrossRef]
21. Peral, E.; Esteban-Fernandez, D. SWOT Mission Performance and Error Budget. In Proceedings of the 2018 IEEE International Geoscience and Remote Sensing Symposium (IGARSS), Valencia, Spain, 22–27 July 2018; pp. 8625–8628. [CrossRef]
22. Chelton, D.B. The Effects of Uncorrelated Measurement Noise on SWOT Estimates of Sea Surface Height, Velocity, and Vorticity. *J. Atmos. Ocean. Technol.* **2022**, *39*, 1053–1083. [CrossRef]
23. Chelton, D.B. A Postlaunch Update on the Effects of Instrumental Measurement Errors on SWOT Estimates of Sea Surface Height, Velocity, and Vorticity. *J. Atmos. Ocean. Technol.* **2024**, *41*, 865–888. [CrossRef]
24. Jacobs, G.A.; D'Addezio, J.M.; Bartels, B. SWOT Cross-Track Error Characteristics Estimated From Observations. *J. Geophys. Res. Oceans* **2025**, *130*, e2024JC021535. [CrossRef]
25. Wang, J.; Lucas, A.J.; Stalin, S.; Lankhorst, M.; Send, U.; Schofield, O.; Kachelein, L.; Haines, B.; Meinig, C.; Pinkel, R.; et al. SWOT Mission Validation of Sea Surface Height Measurements at Sub-100 km Scales. *Geophys. Res. Lett.* **2025**, *52*, e2025GL114936. [CrossRef]
26. Lichtman, I.D.; Bell, P.S.; Gommenginger, C.; Banks, C.; Calafat, F.M.; Brown, J.; Williams, S.D.P. Evaluating water levels from the Surface Water and Ocean Topography (SWOT) mission in a hyper-tidal coastal and estuarine environment. *Earth Space Sci.* **2025**, *12*, e2024EA004104. [CrossRef]
27. Han, G.; Klymak, J.M.; Ross, T.; Chen, N. Validation of 1-Day Repeat SWOT Measurements Against Tide-Gauge and Glider Data Off Canada's West Coast. *Geophys. Res. Lett.* **2026**, *53*, e2025GL119491. [CrossRef]
28. Ho, A.; Wang, J.; Haines, B.; Wu, A.; Stalin, S. In situ validation of small-scale spatial variability in significant wave height observations from SWOT. *Earth Space Sci.* **2025**, *12*, e2025EA004286. [CrossRef]
29. Turki, E.I.; Islam, M.S.; Lopez Solano, C.; Salameh, E.; Domingues, M.; Mendoza, T.; Aouf, L.; Froideval, L.; Gutierrez Barcelo, D.; Laignel, B.; et al. On the Use of SWOT Altimetry Data for Monitoring Coastal Hydrodynamics. *Int. J. Appl. Earth Obs. Geoinf.* **2025**, *145*, 104982. [CrossRef]
30. Vega-Gimenez, D.; Amores, A.; Paris, A.; Pascual, A. Expanding the coastal observation frontier: SWOT reveals the spatial footprint of storm surges. *Geophys. Res. Lett.* **2025**, *52*, e2025GL117299. [CrossRef]
31. Ardhuin, F.; Molero, B.; Bohé, A.; Nouguier, F.; Collard, F.; Houghton, I.; Hay, A.; Legrésy, B. Phase-resolved swells across ocean basins in SWOT altimetry data: Revealing centimeter-scale wave heights including coastal reflection. *Geophys. Res. Lett.* **2024**, *51*, e2024GL109658. [CrossRef]
32. Ardhuin, F.; Postec, T.; Accensi, M.; Piolle, J.-F.; Dodet, G.; Passaro, M.; De Carlo, M.; Husson, R.; Guitton, G.; Collard, F. Sizing the largest ocean waves using the SWOT mission. *Proc. Natl. Acad. Sci. USA* **2025**, *122*, e2513381122. [CrossRef] [PubMed]
33. Islam, M.S.; Turki, E.I.; Solano, C.L.; Froideval, L.; Chartrand, X.; Matte, P.; Bergsma, E.W.J.; Laignel, B.; Picot, N. Revealing Coastal Storm-Wave Transformations From SWOT HR Observation: The English Channel Case Study. *Geophys. Res. Lett.* **2026**, *53*, e2025GL121115. [CrossRef]
34. Project, S.W.O.T. Surface Water and Ocean Topography (SWOT) Project—Release Note—Version D. KaR. In *Science Data Products*; SWOT Level-2 High-Rate Pixel Cloud (L2_HR_PIXC), Version D; NASA/JPL: Pasadena, CA, USA, 2025. [CrossRef]
35. Hart-Davis, M.G.; Andersen, O.B.; Ray, R.D.; Zaron, E.D.; Schwatke, C.; Arildsen, R.L.; Dettmering, D.; Nielsen, K. Tides in complex coastal regions: Early case studies from wide-swath SWOT measurements. *Geophys. Res. Lett.* **2024**, *51*, e2024GL109983. [CrossRef]
36. Villas Bôas, A.B.; Marechal, G.; Bohé, A. Observing interactions between waves, winds, and currents from SWOT. *Geophys. Res. Lett.* **2025**, *52*, e2024GL114331. [CrossRef]
37. Verdy, A.; Gille, S.T.; Cornuelle, B.D.; Gopalakrishnan, G.; Mazloff, M.R. SWOT Observations Constrain a 4D-Var State Estimate of the California Current System. *Earth Space Sci.* **2026**, *13*, e2025EA004931. [CrossRef]

Disclaimer/Publisher's Note: The statements, opinions and data contained in all publications are solely those of the individual author(s) and contributor(s) and not of MDPI and/or the editor(s). MDPI and/or the editor(s) disclaim responsibility for any injury to people or property resulting from any ideas, methods, instructions or products referred to in the content.